November 12, 2003

Environmental Snapshots for Satellite Multi-Angle Aerosol Retrieval Validation During the ACE-Asia Field Campaign

Authors:

Ralph Kahn, Jim Anderson, Theodore L. Anderson, Tim Bates, Fred Brechtel, Antony Clarke, Ellsworth Dutton, Richard Flagan, Robert Frouin, Hajime Fukushima, Brent Holben, Steve Howell, Barry Huebert, Anne Jefferson, Haflidi Jonsson, Kip Carricol, Olga Kalashnikova, Jiyoung Kim, Sang-Woo Kim, Pinar Kus, Wen-Hao Li, John M. Livingston, Sarah Masonis, Cameron McNaughton, John Merrill, Sonoyo Mukail, Toshiyuki Murayama, Teruyuki Nakajima, Patricia Quinn, Jens Redemann, Mark Rood, Phil Russell, Itaru Sano, Beat Schmid, John Seinfeld, Nobuo Sugimoto, Jian Wang, Ellsworth J. Welton*, Jae-Gwang Won, Soon-Chang Yoon

Submission to: Journal of Geophysical Research - Atmospheres

On five occasions spanning the ACE-Asia field experiment in spring 2001, the multi-angle imaging MISR instrument, flying aboard the NASA Earth Observing System's Terra satellite, took quarter-kilometer data over a 400-km-wide swath, coincident with high-quality observations by multiple instruments on two or more participating surface and airborne platforms. The cases capture a range of clean, polluted, and dusty aerosol conditions. They represent some of the best opportunities during ACE-Asia for comparative studies among intensive and extensive aerosol observations in their environmental context. We inter-compare related measurements and discuss the implications of apparent discrepancies for each case, at a level of detail appropriate to the analysis of satellite observations. With a three-stage optical modeling process, we synthesize data from multiple sources into layer-by-layer snapshots that summarize what we know about the state of the atmosphere and surface at key locations during each event, to be used for satellite vicarious calibration and aerosol retrieval validation.

Aerosols within a few kilometers of the surface were composed primarily of pollution and Asian dust mixtures, as expected. Accumulation and coarse-mode particle size distributions varied little among the events studied, but column aerosol optical depth changed by more than a factor of four, and the near-surface proportion of dust ranged from about 25% to 50%. The amount of absorbing material in the sub-micron fraction was highest when near-surface winds crossed Beijing and the Korean Peninsula, and was considerably lower for all other cases.

Ambiguities remain in segregating size distributions by composition; having simultaneous single scattering albedo measurements at more than a single wavelength would significantly reduce the resulting optical model uncertainties, as would integral constraints from surface and atmospheric radiative flux observations. The consistency of component particle micro-physical properties among the five events, even in this relatively complex aerosol environment, suggests that global, satellite-derived maps of

aerosol-air-mass-type extent, combined with targeted in situ measurements, can provide a detailed global picture of aerosol behavior. Further joint satellite and in situ analysis is needed to assess the spatial variability of both intensive and extensive aerosol properties within aerosol air masses in two spatial dimensions.

* Co-Author: Dr. E. J. Welton
NASA GSFC Code 912
Ellsworth.J.Welton@nasa.gov

Environmental Snapshots for Satellite Multi-Angle Aerosol Retrieval Validation During the ACE-Asia Field Campaign

Ralph Kahn[1], Jim Anderson[2], Theodore L. Anderson[3], Tim Bates[4], Fred Brechtel[5], Antony Clarke[6], Ellsworth Dutton[7], Richard Flagan[8], Robert Frouin[9], Hajime Fukushima[10], Brent Holben[11], Steve Howell[6], Barry Huebert[6], Anne Jefferson[7], Haflidi Jonsson[12], Kip Carrico[13], Olga Kalashnikova[1], Jiyoung Kim[14], Sang-Woo Kim[15], Pinar Kus[16], Wen-Hao Li[1], John M. Livingston[17], Sarah Masonis[3], Cameron McNaughton[6], John Merrill[18], Sonoyo Mukai[19], Toshiyuki Murayama[20], Teruyuki Nakajima[21], Patricia Quinn[4], Jens Redemann[22], Mark Rood[16], Phil Russell[23], Itaru Sano[19], Beat Schmid[22], John Seinfeld[8], Nobuo Sugimoto[24], Jian Wang[25], Ellsworth J. Welton[11], Jae-Gwang Won[15], Soon-Chang Yoon[15]

[1]Jet Propulsion Laboratory, California Institute of Technology, 4800 Oak Grove Drive, Pasadena CA 91109 USA

2 Dept. of Mechanical and Aerospace Engineering, Arizona State University, University Blvd., Tempe, AZ 85287 USA

3 Joint Institute for the Study of the Atmosphere and Oceans, University of Washington, Seattle, WA 98195 USA

4 NOAA PMEL, 7600 Sand Point Way NE, Seattle, WA 98115 USA

5 Brechtel Mfg. Inc., 1789 Addison Way, Hayward, CA. 94544 USA

6 Department of Oceanography, University of Hawaii, 1000 Pope Road, Honolulu, HI 96822 USA

7 NOAA/CMDL, 325 Broadway, Boulder, CO 80305 USA

8 Department of Chemical Engineering, California Institute of Technology, 1200 E. California Blvd., Pasadena CA 91125 USA

9 Scripps Institution of Oceanography, University of California at San Diego, 8605 la Jolla Shores Dr., La Jolla, CA 92037 USA

10 School of High-Technology for Human Welfare, Tokai University, 317 Nishino, Numazu, 410-0395 Japan

11 NASA Goddard Space Flight Center, Greenbelt, MD 20771 USA

12 Center for Interdisciplinary Remotely Piloted Aircraft Studies (CIRPAS), Naval Postgraduate School, 3240 Imjin Road, Hangar #510, Marina, CA 93933 USA

13 Atmospheric Sciences Department, Colorado State University, Ft. Collins, CO 80523 USA

14 Meteorological Research Institute, Korea Meteorological Administration, 460-18 Shindaebang-Dong, Dongjak-gu, Seoul 156-720, South Korea

15 School of Earth and Environmental Sciences, Seoul National University, San 56-1, Shillim-dong, Kwanak-gu, Seoul 151-742, South Korea

16 Dept. of Civil and Environmental Engineering, University of Illinois at Urbana-Champaign, 205 N. Mathews Ave., Urbana, IL 61801 USA

17 SRI International, 333 Ravenswood Avenue, Menlo Park, CA 94025-3453

18 Graduate School of Oceanography, University of Rhode Island, South Ferry Rd., Narragansett, RI 02882 USA

19 Faculty of Science and Technology, Kinki University, Higashi-Osaka 577-8502, Japan

20 Division of Physics, Tokyo University of Mercantile Marine, 2-1-6 Etchujima, Koto-ku, Tokyo, 135-8533, Japan

21 Center for Climate System Research, University of Tokyo, 4-6-1Komaba, Meguro-ku, Tokyo 153, Japan

22 Bay Area Environmental Research Institute, 560 3rd Street West, Sonoma, CA 95476

23 NASA Ames Research Center, MS 245-5, Moffett Field CA 94035 USA

24 Atmospheric Environment Division, National Institute for Environmental Studies, 16-2 Onogawa, Tsukuba Ibaraki 305-0053, Japan

25 Atmospheric Science Division, Brookhaven National Laboratory, Brookhaven NY

For: The Journal of Geophysical Research, Atmospheres

Special ACE-Asia Issue B

November, 2003

Abstract

On five occasions spanning the ACE-Asia field experiment in spring 2001, the multi-angle imaging MISR instrument, flying aboard the NASA Earth Observing System's Terra satellite, took quarter-kilometer data over a 400-km-wide swath, coincident with high-quality observations by multiple instruments on two or more participating surface and airborne platforms. The cases capture a range of clean, polluted, and dusty aerosol conditions. They represent some of the best opportunities during ACE-Asia for comparative studies among intensive and extensive aerosol observations in their environmental context. We inter-compare related measurements and discuss the implications of apparent discrepancies for each case, at a level of detail appropriate to the analysis of satellite observations. With a three-stage optical modeling process, we synthesize data from multiple sources into layer-by-layer snapshots that summarize what we know about the state of the atmosphere and surface at key locations during each event, to be used for satellite vicarious calibration and aerosol retrieval validation.

Aerosols within a few kilometers of the surface were composed primarily of pollution and Asian dust mixtures, as expected. Accumulation and coarse-mode particle size distributions varied little among the events studied, but column aerosol optical depth changed by more than a factor of four, and the near-surface proportion of dust ranged from about 25% to 50%. The amount of absorbing material in the sub-micron fraction was highest when near-surface winds crossed Beijing and the Korean Peninsula, and was considerably lower for all other cases.

Ambiguities remain in segregating size distributions by composition; having simultaneous single scattering albedo measurements at more than a single wavelength would significantly reduce the resulting optical model uncertainties, as would integral constraints from surface and atmospheric radiative flux observations. The consistency of component particle micro-physical properties among the five events, even in this relatively complex aerosol environment, suggests that global, satellite-derived maps of aerosol-air-mass-type extent, combined with targeted *in situ* measurements, can provide a detailed global picture of aerosol behavior. Further joint satellite and *in situ* analysis is needed to assess the spatial variability of both intensive and extensive aerosol properties within aerosol air masses in two spatial dimensions.

1. Introduction

ACE-Asia, the Aerosol Characterization Experiment, took place over Japan, Korea, and China and the surrounding waters, in spring 2001. Over 400 researchers participated, supporting multiple instrumented aircraft, ships, and land surface environmental measuring stations [*Huebert et al.*, 2003a, b]. One reason for bringing so many resources to bear on a single region is the possibility of simultaneously characterizing key attributes of the surface and atmosphere on scales from tens of meters to tens of kilometers. Such data allow us to grasp the aggregated contributions from many parts of the environment simultaneously, essential for studies ranging from column radiative closure [e.g., *Schmid et al.*, 2003a, *Redemann et al.*, 2003a] to satellite aerosol retrieval validation.

This paper is aimed at satellite aerosol retrieval validation, with an eye toward the longer-term goal of combining the frequent, synoptic coverage made possible by satellite-borne instruments with the detailed particle properties that can only be obtained from *in situ* measurements. Aerosol retrieval validation efforts for the new generation of instruments flying aboard the NASA Earth Observing System (EOS) satellites [e.g., *Diner et al.*, 2001, *Remer et al.*, 2002] rely heavily on the network of sun photometers organized by the Aeronet program [*Holben et al.*, 1998]. Aeronet data are of great value for statistical validation analyses because of their extensive spatial and temporal coverage, uniform data acquisition and analysis approach, and timely accessibility; they are included in this study as well. But the detailed interpretation of Aeronet data alone for satellite validation suffers from some limitations. (1) Surface conditions in the vicinity of most Aeronet sites are not well characterized; they represent lower boundary conditions critical to quantitatively assessing satellite retrieval sensitivity. (2) Particle vertical distribution, another issue for assessing retrieval sensitivity, is also unavailable for most sites. (3) The ability of the Aeronet algorithm to identify thin, uniform cirrus is an issue. (4) Although Aeronet measurements provide time series at a fixed point, assumptions about isotropy and homogeneity must be made to use them for assessing two-dimensional spatial variability relevant to satellite observations. (5) When discrepancies arise between the satellite and Aeronet observations, additional meteorological data to help resolve the differences are usually lacking.

Efforts are being made to address the limitations in the monitoring station observation suite, but for the times and places where they exist, field campaign data, such as those obtained during ACE-Asia, go a long way toward filling the gaps in this picture. The measurements studied here represent a synthesis of data taken from multiple platforms. Two aircraft participated, the National Science Foundation /National Center for Atmospheric Research (NSF/NCAR) C-130 and the Center for Interdisciplinary Remotely Piloted Aircraft Studies (CIRPAS) Twin Otter (TO), along with the National Oceanographic and Atmospheric Administration (NOAA) Research Vessel Ronald H. Brown (RB). Instrumented ground stations at Amami Island, Japan and at Gosan on Jeju Island, Korea, also contributed coincident data. Our field sampling strategy was to fly the aircraft near the surface during satellite overpasses, so airborne sun photometers could measure total column spectral aerosol optical thickness (AOT) corresponding to that seen by the satellite, while *in situ* aerosol physical and chemical experiments collected samples of boundary layer air. A minimum of 30 minutes in a typical aerosol layer was required for some airborne instruments to obtain adequate samples. Before and/or after the near-surface legs were flown, the aircraft performed vertical profiles that yielded atmospheric structure. When possible, upper-level aerosol layers identified in the profiles were sampled during subsequent level legs. And in many cases we were able to target aircraft operations to the vicinity of a surface station.

We focus on five occasions during ACE-Asia when MISR, the Multi-angle Imaging SpectroRadiometer flying aboard the EOS Terra satellite [*Diner et al.*, 1998], took data over a 400-km-wide swath coincident with high-quality, quantitative observations by two or more participating surface and airborne platforms (Table 1). In four cases each, the C-130 and Twin Otter made measurements within the MISR field-of-view; for two of these, the two research aircraft flew in close proximity. The Ronald H. Brown made observations coincident with MISR on three occasions, once in close proximity to the C-130, and once within a few hundred kilometers of the Twin Otter. The Gosan surface station fell within the MISR field-of-view on April 16, with the Twin Otter nearby, and on May 02, when the C-130 was in the immediate vicinity. And the Amami surface station is covered twice in this data set, though it is always more than a few hundred kilometers from any other platform. Figure 1 illustrates the five events with MISR nadir images of the study regions. The locations of the key ACE-Asia platforms at the time of overflight are labeled.

These cases capture a range of clean, polluted, and dusty aerosol conditions, and represent a rich data set for many applications. Regarding MISR validation, they allow us to critically test key assumptions made in the aerosol retrievals about particle and ocean surface properties [*Martonchik et al.*, 1998; *Kahn et al.*, 2001a,b], and to improve the algorithms based on the results. We can then assess the sensitivity of the upgraded retrievals to the range of environmental factors measured in the field.

In this paper, we take a critical initial step by assembling snapshots of atmospheric and surface conditions at key locations during these five events, based on the multi-platform data. The derived optical models and associated uncertainties provide the ground truth for follow-on satellite-aerosol-retrieval validation studies. Section 2 gives brief descriptions of the instruments and measurement techniques involved, along with references to more detailed discussions of each. In Section 3, we present the best accounting we can of the environment in the five cases. We discuss inter-comparisons among field measurements at the level of detail appropriate to validating satellite retrievals, point out any discrepancies, and suggest what assumptions or additional data might help resolve them. In Section 4 we produce synthesis optical models for each aerosol layer for each event. In the final section, we discuss how the ACE-Asia cases presented here will be used for a range of combined satellite and field-measurement aerosol studies in subsequent papers.

2. Measurement Overview

More than forty instruments contributed to this study (Table 2). They were distributed among six platforms: the Terra satellite, the C-130 and Twin Otter aircraft, the Research Vessel Ronald H. Brown, and the Gosan and Amami surface stations. This section offers brief descriptions of the key instruments aboard each platform, highlighting the important points needed to inter-compare results. Detailed discussion of the instruments and measurement techniques, as well as more extensive summaries of their results during the ACE-Asia campaign, are given in the references. In this and subsequent sections, the following abbreviations and symbols are used: RH for relative humidity, AOT for aerosol optical thickness, AOT_{col} to explicitly indicate total column AOT, σ_{ep} for extinction coefficient, σ_{sp} for total scattering coefficient, σ_{bsp} for hemispheric back-scattering coefficient, b for hemispheric backscatter fraction ($=\sigma_{bsp}/\sigma_{sp}$), σ_{ap} for absorption coefficient, SSA for single scattering albedo ($=\sigma_{sp}/\sigma_{ep}$), β_p for 180° back-scatter coefficient (used to interpret Lidar measurements), and S_a for extinction-to-180°-backscatter ratio ($=\sigma_{ep}/\beta_p$). Ångström exponent is calculated from two wavelengths as:

$$A_{xp}(\lambda_1,\lambda_2) = \frac{-\ln\left[\sigma_{xp}(\lambda_1)/\sigma_{xp}(\lambda_2)\right]}{\ln\left[\lambda_1/\lambda_2\right]} \qquad (1)$$

where the subscript xp may be ep if extinction or sp if scattering coefficients are used. When a single λ is given, A_{xp} was evaluated as the slope of a least-squares fit to available data at multiple wavelengths. Similarly, the hygroscopic growth factor, which describes how particle cross-section changes with RH, is given as:

$$f_{xp}(RH_1,RH_2) = \frac{\sigma_{xp}(RH_1)}{\sigma_{xp}(RH_2)} \qquad (2)$$

where xp may be sp or bsp if total or back-scattering coefficients are used, RH_1 may be ambient, and RH_2 is low-RH reference value. The relevant wavelengths are either given in Table 2 or are indicated in parentheses after the symbol, in nm. The unit usually used for extinction, absorption, or scattering coefficients, Mm^{-1} (inverse-mega-meters), converts to optical depth when multiplied by the path length. OC is used for organic carbon, EC for

elemental carbon, and *nss-sulfate* for non-sea-salt sulfate. *DMA* represents Differential Mobility Analyzer, *APS* is Aerodynamic Particle Sizer, *OPC* is Optical Particle Counter, *PSAP* is Particle Soot Absorption Photometer, *IPA* is Individual Particle Analysis, *LTI* is Low Turbulence Inlet, *AATS* is Ames Airborne Tracking Sunphotometer, and *MPL* is Micro-Pulse Lidar. The compass points are abbreviated in the standard way (N, NNE, NE, ENE, etc.). Unless indicated otherwise, component particle sizes are parameterized as area-weighted, log-normal distributions:

$$dN_a(D)/d\log_{10}(D) = \frac{1}{C}\exp\left[-\frac{\log_{10}^2\left(\frac{D}{D_c}\right)}{2\log_{10}^2\sigma}\right] \qquad (3)$$

where

$n(D)$ is the number of particles per unit volume at diameter D, D_c is the characteristic diameter of the distribution, σ is the distribution characteristic width, and C is a normalization constant, obtained so the integral of $dN_a(D)$ from D_1 to D_2, the lower and upper limits of the size distribution considered, equals one. When the size range is evaluated from zero to infinity, $C = \sqrt{2\pi}\log_{10}\sigma$, though most measurements are interpreted using this normalization even though D_1 is greater than 0 and D_2 is finite.

2.1. MISR aboard the Terra satellite

MISR produces 36 simultaneous views of Earth, in a combination of nine angles varying from +70°, through nadir, to –70° in the along-track direction, in four spectral bands [*Diner et al.*, 1998]. It takes seven minutes for all nine MISR cameras to view a fixed line on the surface, which sets the effective temporal resolution for coincident observations. At mid-latitudes, a given location is imaged about once per week in Global Mode, providing 275 m resolution data in all four nadir channels, and in the red channels of the other eight cameras. The remaining 24 channels of data are averaged on board the spacecraft to 1.1 km resolution. For each MISR event day during ACE-Asia, we also designated a MISR Local Mode site, 300 km along-track and 400 km cross-track, over which data were acquired at 275 m resolution in all 36 channels.

Pre-launch theoretical studies indicated that MISR spectral radiances, measured at precisely known air-mass factors ranging from one to three, could provide tight constraints on AOT_{col} over land and water. And along with the wide range of scattering angles sampled (about 50° to 160° at mid-latitudes), MISR would offer constraints on particle shape, size distribution, and composition, particularly over dark, uniform ocean surfaces [*Kahn et al.*, 2001a; 1998; *Martonchik et al.*, 1998]. If these expectations are met, global maps of aerosol amount and of aerosol air mass type (in about a dozen broad classes) can be derived routinely from MISR data. Whereas others instruments involved in this study rely on well-established measurement techniques, the sensitivity of aerosol retrievals based on satellite multi-angle imaging remains to be assessed using actual data. In addition, the assumptions made in the retrieval algorithm about aerosol component particle properties, scene variability, and other factors, must be critically tested and refined. The current study represents one important step toward addressing these validation issues.

2.2. Nephelometers aboard the C-130

A suite of instruments operating downstream of the LTI on the C-130 [*Lafleur*, 1998] was used to measure aerosol visible light scattering and absorbing properties [*Anderson et al*, 2003a; b]. σ_{sp} and σ_{bsp} were measured at three wavelengths, using two integrating nephelometers (model 3563, TSI, Inc., St. Paul, MN); one measured total sampled aerosol while the second measured only sub-micron particles (defined as aerodynamic diameter less than 1 micron at low RH). Both operated at RH < 45%. To provide information on aerosol hygroscopicity, a second pair of single-wavelength nephelometers (model M903, Radiance Research, Seattle, WA) operated at low (<45%) and high (85%) RH, respectively, yielding the dependence of scattering on RH, assuming the dependence is exponential in form [*Kasten*, 1969]. σ_{ap} was measured for both total and sub-micron aerosol, at low RH and 550 nm wavelength, with a pair of differential transmission absorption photometers (model PSAP, Radiance Research, Seattle, WA), and β_p at low RH was measured with a modified TSI nephelometer [*Doherty et al.*, 1999]. This combination of measurements permits the following quantities to be derived: (i) σ_{sp} at ambient *RH* (which generally compares well with an independent measurement by differential sun-photometry; *Redemann et al.*, this issue), (ii) the scattering, back-scattering, and absorption components of extinction, (iii) the sub- and super-micron particle contributions to the components of extinction, and (iv) basic optical

properties: *SSA*, *b*, S_a, and A_{sp}. Neph-130 and PSAP-130 data were calibrated and corrected for instrumental non-idealities according to established recommendations [*Anderson and Ogren*, 1998; *Bond et al.*, 1999]. Uncertainties associated with noise, calibration, correction factors, and RH-adjustments were used to determine 95% confidence values for each reported quantity.

2.3. *OPC, APS,* and Chemical Samplers aboard the C-130

Two instruments aboard the C-130 measured particle size distributions over optically active diameter ranges during flight. An *OPC* (modified LAS-X ASASP) detected particles from 120 nm to 15 μm, and an *APS* (TSI model 3020) recorded 0.8 to 12 μm particles. Both drew air from the same *LTI* as the nephelometers. During level flight, sample air to the *OPC* was periodically diverted through heated tubes to give some indication of the chemical composition of the particles [*Clarke*, 1991]. The *APS* ran in correlated mode to minimize the influence of "ghost particles" caused by re-circulation within the sensing volume. It operated at the same *RH* as the aerosol inlet, lower than ambient. *OPC* samples were dried further by mixing with filtered and dessicated air. The *OPC*, calibrated with spheres of known refractive index, provides optically effective sizes (*OES*) for all particle shapes and compositions. Optical properties can be calculated directly from *OES* for particles having refractive indices near the calibration value (e.g., Asian dust); for wet and absorbing aerosols, corrections for refractive index differences are made, based on measured composition. Estimated uncertainties in derived ambient extinction are about 15% [*Clarke et al.*, 2002]; additional uncertainties are introduced when converting *OES* to mass equivalent size.

Aerosol chemical composition was measured with three samplers. *OC* and *EC* were collected on quartz filters in a PC-BOSS sampler designed to minimize positive and negative vapor artifacts. The filters were analyzed using a Sunset Labs thermal/optical instrument and the NIOSH technique [*Huebert et al.*, 2003c]. Bulk inorganic chemical composition was measured by collecting aerosols in a total aerosol sampler (*TAS*) mounted outside the fuselage. It used a replaceable diffuser liner cone and Teflon filter to collect every particle that enters its tip, to be extracted for ion chromatography analysis. By sampling iso-kinetically, *TAS* avoids any inlet or plumbing artifacts, even for large dust particles. The third sampler is an eight-position multiple micro-orifice cascade impactor (*MOI*) made by MSP Corp., which received air from a dedicated low-turbulence inlet, LTI. Its aluminum substrates and backup filters were also analyzed by ion chromatography. Efficiency corrections were made to the impactor results based on *Berner et al.* [1979].

For the current study, these data were interpreted as follows: Coarse mode particles are partitioned between dust and sea salt, based on the calcium to sodium ion abundance ratio. Dust is assumed to have index of refraction 1.58-0.0006i and to be non-hygroscopic, whereas sea salt index of refraction and hygroscopicity are obtained from simultaneous levitated drop experiments [*Tang and Munkelwitz*, 1991]. The sub-micron particles are assumed to be homogeneous spheres, a mix of four components: sulfate and *OC* comprising the volatile fraction, and for the refractory component, *EC* and dust or fly-ash, with the added constraint that the volume distribution of dust should diminish for decreasing particle size. The hygroscopicity of the volatile fraction is taken as equal to that derived for the pollution component in the INDOEX and ACE-2 experiments [*Clarke et al.*, 2002]. Many of these assumptions will be relaxed in future analyses of the ACE-Asia data.

2.4. *IPA* Samples taken aboard the C-130 and Ronald H. Brown

Aerosol samples for individual-particle analysis by scanning electron microscope (*SEM*) and transmission electron microscope (*TEM*) were collected with filter and micro-impactor systems connected to the low turbulence inlet on the NCAR C-130. *SEM* samples were collected with two Programmable Streaker Samplers (PIXE International) configured for one-stage filtration on polycarbonate membranes. *TEM* samples were collected on 3 mm grids with a three-stage micro-impactor (California Measurements). One or more sample sets was collected on each level leg of flight. *SEM* and *TEM* samples were also continuously collected using Streakers on the Ron Brown; sample duration was 2 hours.

Inorganic particle composition, size, and shape are measured with an automated *SEM* [*Anderson et al.*, 1996]. Minimum particle size is about 100 nm. Black carbon particles are examined manually with a field emission *SEM*; minimum particle size is about 10 nm. *TEM* is used to examine fine-scale structure and mixing states of particles as small as 10 nm. The *TEM* also allows analysis of nitrates that survive in high vacuum. However, low collection efficiency limits the examination of particles smaller than 50 nm.

2.5. *AATS* Instruments aboard the C-130 and Twin Otter

The 6-channel NASA Ames *AATS-6* operated on 15 of the 19 research flights of the C-130; its 14-channel counterpart, *AATS-14*, flew successfully on 19 research flights of the Twin Otter. *AATS-6* and *AATS-14* measure direct solar beam transmission at 6 and 14 wavelengths (380 to 1021 and 354 to 1558 nm, respectively). In both *AATS* instruments, azimuth and elevation motors controlled by differential sun sensors rotate a tracking head so as to lock on to the solar beam and keep detectors normal to it. The tracking head of each instrument mounts external to the aircraft skin, to minimize blockage by aircraft structures and also to avoid data contamination by aircraft-window effects. Each channel consists of a baffled entrance path, interference filter, photodiode detector, and preamplifier, which are temperature-controlled to avoid thermally induced calibration changes. The data yield *AOT* spectra and column water vapor. Vertical differentiation of these data in suitable flight patterns yields extinction spectra and water vapor concentration. Examples are given in *Russell et al.*, 1999, *Schmid et al.*, 2000, *Livingston et al.*, 2003, *Schmid et al.*, 2003a,b, *Redemann et al.*, 2003b. *AATS AOT* is reported in this paper at wavelengths common to other instruments by interpolating along linear (for AATS-6) or quadratic (for AATS-14) fits to $\log(AOT_{ap})$ vs. $\log(\lambda)$. $A_{ap}(\lambda)$ is derived as the slope of the line in $\log(extinction)$ vs. $\log(\lambda)$ space, passing through *extinction*(380) and *extinction* (1020).

Pre- and post-mission radiometric calibration for the ACE-Asia field campaign was determined via Langley plots using data taken at the high-altitude Mauna Loa Observatory in March and June of 2001, respectively. For *AATS-14*, comparison of pre- and post-mission calibration constants, time-interpolation from pre- to post-mission values, and inspection of high-altitude *AOT* spectra during the campaign, produce an effective calibration that was less than 0.6% different from pre-mission values in 11 channels and less than 1.5% different in the remaining three channels. For *AATS-6*, the same procedure, in addition to in-flight and ground-based comparisons with *AATS-14*, reveals that pre-mission calibration constants need to be used for flights until April 12, 2001 (C-130 flight RF07). Thereafter, post-mission calibration is applied. Because of occasional poor tracking performance of *AATS-6*, a tracking uncertainty of 2% is added to the uncertainties in the calibration constants. Methods for *AATS* data reduction and error analysis can be found in *Russell et al.*, 1993 and *Schmid et al.*, 2003b. Details that pertain to the analysis of *AATS* data obtained in ACE-Asia are described in *Schmid et al.*, 2003a, for *AATS-14* and *Redemann et al.*, 2003b, for *AATS-6*.

2.6. *DMA* and *APS* aboard the Twin Otter

Aerosol size distributions were measured by *DMA* systems and *APS* on board Twin Otter during ACE-Asia. Two *DMA* systems operated in parallel inside the main cabin of the Twin Otter [*Wang et al.*, 2003]. One measured dry aerosol size distribution by passing the aerosol flow through a Nafion drier prior to the measurement; the other operated at ambient RH, using an active RH controller [*Wang et al.*, 2003]. The size measurement sections of the two systems downstream of the drier and active RH controller were identical. The main components of the measurement section were a cylindrical *DMA* (TSI Inc., model 3081) and a condensation particle counter (TSI Inc., model 3010) having a 50% counting efficiency at 10 nm. All the flows associated with the *DMA* are monitored and maintained by feedback controllers to compensate for environmental changes during airborne measurement. Using the scanning mobility technique, each *DMA* system generates a size distribution from 15 nm to 1 micron diameter every 100 sec. The aerosol sample flows for the *DMA* systems were drawn from the Twin Otter community inlet, which was shared by other instruments. For the particle size range measured by the *DMA* systems, the aerosol transmission efficiency through the community inlet has been established to be 100%. Data from the *DMA* systems were analyzed using the data inversion procedure described by *Collins et al.* [2002].

An *APS* (TSI model 3320), having a measurement range of 0.5 to 20 microns aerodynamic diameter, was mounted under the left wing of the Twin Otter. The *APS* infers particle size by measuring the velocity of particles inertially accelerated in an expanding air stream; large particles undergo smaller acceleration and reach lower velocity than small particles. To derive aerosol size from *APS* measurements, particle size and density are required; the procedure used is described in detail by *Wang et al.* [2002]; the overall uncertainties amount to about 5% for *DMA* size, 10% for *APS* size, and 10% for *DMA* and APS particle concentration.

2.7. Sun Photometer and Aerosol *In Situ* Chemical and Physical Properties Measurements aboard the Ronald H. Brown

AOT. *AOT* was derived from a 5-channel hand-held Microtops sun photometer (Solar Light Co.), having built-in pressure and temperature sensors, and an associated global positioning system (*GPS*) [*Quinn et al.*, 2002]. To reduce pointing errors caused by ship motions, the

maximum voltage from a one-minute sequence of 10-second measurements was kept. In converting the raw signal voltages to *AOT*, corrections were applied for Rayleigh scattering, ozone opacity, and the effect of Earth's curvature on air mass. The instrument was calibrated using a Langley plot approach, prior to the cruise and again one year later. Calibration constants in all channels differed by less than 0.9% between the two calibrations, representing about 0.01 variation in *AOT*.

Inlet. Aerosol particles were sampled 18 m above the sea surface through a heated mast designed to maintain iso-kinetic flow and to minimize the loss of super-micron particles. The lower 1.5 m of the mast was heated to dry the aerosol to an *RH* of 55 ± 5%, allowing constant instrumental size cuts through variations in ambient *RH*. Fifteen 1.9 cm diameter electrically conductive polyethylene or stainless-steel sampling tubes extend into this heated zone to direct the air stream at flows of 30 l min^{-1} to the various aerosol sizing/counting instruments and impactors [*Quinn et al.*, 2001; *Bates et al.*, 2001; 2003].

Aerosol number size distributions and concentrations. Details of the particle number size distributions and concentrations can be found in *Bates et al.* [2001]. Briefly, total particle number concentrations were measured with a condensation particle counter (*CPC*, model 3010, TSI, St. Paul, MN) operated directly off one of the 1.9 cm sampling tubes. The same tube supplied ambient air to a differential mobility particle sizer (*DMPS*) located inside a humidity-controlled box at the base of the sampling mast. Data were collected in 27 size bins having midpoints ranging from 22 and 900 nm diameter.

Another 1.9 cm tube was connected to an *APS* (model 3320, TSI) located in the humidity-controlled box measuring the number size distribution between 0.6 and 9.6 μm aerodynamic diameter. The *APS* data were converted from aerodynamic diameters to geometric diameters at 55% RH using calculated densities and the water masses associated with the inorganic ions at 33 and 55% RH. The densities and associated water masses were calculated with a thermodynamic equilibrium model using the measured chemical data [*Quinn et al.*, 2001], and the combined *DMPS* and *APS* number distributions were converted to surface area distributions. The derived number size distributions are uncertain to about ± 20%, dominated by instrumental particle sizing errors and counting errors due to flow instabilities.

Aerosol scattering and absorption coefficients. σ_{sp} was measured with an integrating nephelometer (Model 3563, TSI Inc.) at 55% RH, at three wavelengths. Values were corrected for offset [*Anderson and Ogren*, 1998], and for nephelometer angular non-idealities, including truncation errors and non-lambertian response [*Quinn et al.*, 2001]. For a 30 minute averaging time, a quadrature sum of errors yielded absolute uncertainties of 4.1 and 20 Mm^{-1}, corresponding to low and high values of σ_{sp} equal to 24 and 110 Mm^{-1}, respectively. σ_{ap} was measured at 565 nm and 55% RH by monitoring the change in transmission through a filter with a *PSAP* (Radiance Research) and reported at 550 nm [*Quinn et al.*, 2001]. A quadrature sum of errors yields absolute uncertainties of 0.38 and 2.8 Mm^{-1} for σ_{ap} equal to 0.68 and 13 Mm^{-1}, respectively, for a 30 minute averaging time. *Neph-RB* and *PSAP-RB* values are reported at 0°C, 1013 mb, and 55 ± 5% RH.

Independently, σ_{sp}, σ_{bsp}, and their *RH* dependence were measured with a scanning nephelometry system (*NephRH-RB*, *Carrico et al.*, 2003), using the same particle size limits and wavelengths as Neph-RB. One nephelometer (model 3563, TSI Inc.) operated at "dry" conditions (*RH* 19±5%), while two downstream nephelometers (model 3563, TSI, Inc. and model M903, Radiance Research, Inc.) operated with controlled *RH* that scanned between 35% and 85%. Increasing RH scans started from the "dry" aerosol condition and decreasing *RH* scans started from the "hydrated" aerosol condition to examine the aerosol's deliquescence, crystallization, hysteresis, and metastable properties. Corrections were made for particle loss (~5%) and nephelometer non-idealities [*Anderson and Ogren*, 1998], and adjusted to 0° C and 1013 mbar. Results at controlled *RH* values are provided for σ_{sp} and σ_{bsp} as $f_{sp}(RH,19 \pm 5\%)$ and as $f_{bsp}(RH,19 \pm 5\%)$; results are given for λ = 550 nm and particle diameter < 10 μm unless specified otherwise. Comparing σ_{sp} values from the *Neph-RB*, which only warms the ambient sample an average of 4°C, to σ_{sp} values from the *NephRH-RB*, gives direct evidence about the state of hydration of the aerosol at ambient conditions. $A_{sp}(450,550)$, $b(550)$, and *SSA(550)* were also derived, and reported at ambient conditions. σ_{ap} at *RH* ~ 55% from the PSAP-RB were used to calculate *SSA*.

Mass fractions of aerosol chemical components. Sub- and super-micron aerosol chemical component mass fractions were calculated from measured chemical component concentrations, and filters weighed before and after sample collection [*Quinn et al.*, 2001]. Mass fraction uncertainties at the 95% confidence level are based on a quadratic sum of

chemical concentration uncertainties, along with gravimetrically determined mass. Uncertainties for the inorganic ionic components (nss-$SO^{4=}$, NH^{4+}, sea salt, and NO_3^-) range from ±3% to ±7%. Uncertainties are higher for *OC* (±25%), *EC* (±10%), and dust (±20%).

2.8. *MPL* aboard the Ronald H. Brown

The NASA MPLNet project [*Welton et al.*, 2001] deployed a unit aboard the RB, forward of the vessel's stacks to limit any influence from the ship engine exhaust, and was housed inside a climate-controlled sea container. The instrument is a single-channel, semi-autonomous, eye-safe Lidar system that yields vertical structure of clouds and aerosols [*Spinhirne et al.*, 1995]. Installation of the *MPL* and data processing were identical to those described by *Welton et al.* [2002] for the INDOEX 1999 cruise. Raw *MPL* data, acquired at 1 minute time resolution and 75 m vertical resolution, were converted into uncalibrated Lidar signals [*Campbell et al.*, 2002; *Welton and Campbell*, 2002]. Aerosol extinction profiles were calculated using the algorithm described by *Welton et al.* [2000], for times coincident with *Mtps-RB* measurements, that help interpret backscatter in terms of *AOT*. The *Mtps-RB* data were analyzed by the NASA Sensor Intercomparison and Merger for Biological and Interdisciplinary Oceanic Studies (SIMBIOS) project [*Miller et al.*, in press].

2.9. SIMBAD spectral water reflectance and AOT from the Ronald H. Brown

Diffuse marine reflectance (i.e., the reflectance of the water body) and *AOT* were measured from the bow of the RB by a *SIMBAD* radiometer [*Deschamps et al.*, 2002]. The instrument is portable and does not require the ship to stop. For diffuse marine reflectance, the radiometer is aimed at the ocean surface from the side of the ship lit by the sun, at an angle of 45° from nadir, and a relative azimuth angle of 135°. With the help of a polarizer, this viewing geometry allows one to reduce substantially, skylight reflected by the surface in the instrument's field of view [*Fougnie et al.*, 1999]. For *AOT*, the radiometer is aimed at the sun. The same 2.5° field-of-view optics and the same detectors are used in sun- and sea-viewing modes, but with different electronic gains. The radiometric data is acquired simultaneously in five spectral bands in each mode. To transform water-leaving radiance into water reflectance, downward solar irradiance at the surface is calculated, which can be done accurately under clear skies or when the sun's fractional cloud cover coverage is less than 0.2.

The *AOT* root-sum-square errors, due mostly to calibration uncertainty, is ±0.02, ±0.02, ±0.02, ±0.01, and ±0.01 at 443, 490, 560, 670, and 870 nm, respectively, for an airmass of unity (smaller at higher airmass). The uncertainty in diffuse marine reflectance, due to various factors, especially calibration errors, residual skylight reflection, and polarization of the water body, is ±1.4 10^{-3} (6%), ±1.1 10^{-3} (6%), ±0.4 10^{-3} (8%), and ±0.2 10^{-3} (23%) in the four shorter spectral bands, for an ocean containing 0.1 mg-m^{-3} of chlorophyll-a. No water reflectance is obtained at 870 nm, where the ocean is assumed black. To insure data quality, the instrument was calibrated in sun- and sea-viewing modes before and after the experiment using the Bouguer-Langley method and an integrating sphere, and average calibration coefficients were used in the data processing.

2.10. AERONET Sun Photometers at Gosan and other Surface Stations

AERONET is a collaborative, globally distributed network of identical, seven-channel sun- and sky-scanning spectral radiometers that retrieve column integrated aerosol parameters including *AOT*. Data are taken every 15 minutes (given cloud free conditions), are processed and calibrated through a common data stream, and exhibit nominal accuracy of ±0.01 [*Eck et al*, 1999, *Holben et al*, 1998, *Smirnov et al.*, 2000]. Hourly sky scans are made through the aureole in the almucantar, yielding particle size distribution, phase function, spectral modal *AOT*, spectral *SSA*, and spectral complex index of refraction [*Dubovik and King*, 2001]. Accuracy of retrieved parameters vary according to environmental conditions; however quality-assured data typically yields *SSA* with ±0.03 absolute accuracy, real index of refraction to ±0.02, and a size distribution range from 0.05 to 15 μm [*Dubovik et al.*, 2001].

Sixteen sites were located within the greater Ace Asia study area during the campaign, including Bejing China, Dunhuang China, IMGRASS (NE China), Noto Japan, Osaka Japan, Okinawa Japan, Shirahama Japan, Dalanzadgad Mongolia, Anmyon Is. S. Korea, Gosan S. Korea, Lan-Yu, Is. Taiwan, Wan-Li Taiwan, NCU Taiwan, Midway Is. Hawaii, Mauna Loa Hawaii, and Lanai Hawaii. Data were collected from March to June and posted on the AERONET website: http://aeronet.gsfc.nasa.gov. Observations at Gosan began April 4 and continued through June 20.

2.11. *MPL* at the Gosan Surface Site

Seoul National University deployed a single-channel *MPL* [(SES Inc., USA), *Yoon and Won*, 1998; *Murayama et al.*, 2001] at the Gosan surface site. Background information is given in *Spinhirne* [1995] and *Welton et al.* [2000]. The vertical resolution was adjusted to 30 m, and the *MPL* was set to average and analyze the backscattered signal every 10 minutes. σ_{ap} profiles were retrieved from the signals by the method of *Fernald* [1984] and *Klett* [1981]. From these, the altitude and thickness of Asian dust layers, as well as aerosol optical thickness, are derived.

2.12. *DMA*, *OPC*, Chemical Size Distribution, and *AOT* at the Gosan Surface Site

Intensive measurements of aerosol size, concentration, and chemical composition were obtained from a suite of instruments at Gosan. They included two *DMA*s [*Brechtel et al.*, 1998; *Brechtel and Kreidenweis*, 2000], two *OPC*s, [*Brock et al.*, 2003; *Lee et al.*, 2002], two mass spectrometers providing aerodynamic particle size distributions [*Zelenyuk et al.*, 2001], along with sun photometer and meteorological measurements. All particle number size measurements were conducted at $RH < 30\%$ to remove particle-bound water and facilitate instrument inter-comparisons. Size-resolved particle growth factor, as a function of *RH*, was measured by a Humidified Tandem Differential Mobility Analyzer (HTDMA) [*Brechtel and Kreidenweis*, 2000; *Buzorius et al.*, 2002], to help translate dry size distribution to ambient *RH*. Mobility number size distributions were obtained over the diameter range 0.005-0.6 microns, whereas *OPC* distributions were observed over the diameter range 0.1-25 microns [*Lee et al.*, 2002]. All number size distribution measurements were corrected for size-dependent inlet losses [*Willeke and Baron*, 1993].

Daily-averaged chemical size distributions of sulfate, nitrate, and organic-containing particles from Berner impactors, covered the aerodynamic size range 0.1 to 10 μm. Size-dependent particle density and refractive indices, calculated from the impactor data, were used to adjust the aerodynamic to mobility size and to correct the *OPC* data for index-of-refraction effects, respectively. The use of realistic, size-resolved refractive indices significantly altered the *OPC* diameter and therefore the moments of the *OPC* size distribution.

A ground-based, five-channel sun photometer made *AOT* measurements once per minute. We compare this spectral *AOT* data with observations from the Gosan AERONET and *AATS-6* instruments in Section 3. Meteorological measurements, including surface temperature, *RH*, near-surface wind speed and direction, and atmospheric pressure were sampled once per minute at 10 meter elevation.

2.13. *AOT*, Radiation, and In-situ Aerosol Optical Properties at the Gosan Surface Site

CMDL made *AOT* and surface radiation budget observations complementary to the measurements described in Section 2.12 [*Dutton et al.* 1994; *Dutton and Christy* 1992; *Dutton and Bodhaine* 2001]. The instrumentation included two Carter-Scott six-channel sun photometers and broadband solar radiometers for direct, diffuse, total solar irradiance, all mounted on a Sci-Tech active solar tracker atop a 30 m tower. The instruments were calibrated at CMDL facilities in Boulder Colorado both before and after the one-year deployment. The sun photometers were repeatedly calibrated on-site during the field phase. One-minute average data from all radiometers were derived from 1 Hz sampling; sun photometer sampling was once-per-minute-on-the-minute. The broadband radiometer calibration accuracy is documented in *Ohmura et al.* [1998], with recent enhancements outlined by *Dutton et al.* [2001]. Accuracy of the spectral *AOT* is believed to be approximately 0.02 or 5%, whichever is larger. On-site personnel provided minimal field instrument maintenance and cleaning, and the data were collected several times daily and transferred by phone line to Boulder Colorado for processing.

In addition, σ_{sp} was measured with two nephelometers (Model 3563, TSI, Inc.) at three wavelengths, as a function of scattering angle (7°- 170°, and < 90°) and *RH* (50%-95%). Corrections for noise, instrument drift, calibration and truncation of forward scattered radiation were made according to *Anderson and Ogren* [1998]. σ_{ap} was measured at 565 nm by a Radiance Research *PSAP*, with data corrections for sample area, flow rate, and non-idealities in the manufacturer's calibration based on *Bond et al.* [1999]. Aerosol impactors allowed us to determine σ_{sp} and σ_{ap} separately for sub-micron and sub-10 micron sized aerosol. Detailed descriptions of this instrumentation, its operation, associated uncertainties and variability appear in *Sheridan et al.* [2001] and *Delene and Ogren* [2002]. From these measurements we calculate aerosol intensive properties: *SSA*, $A_{sp}(550,700)$, $f(RH)$, and b.

2.14. Ground-based Atmospheric Column Measurements at Amami-Oshima Island

A portable, six-channel photopolarimeter, PSR-1000, operated at Amami-Oshima Island. PSR-1000 results are interpreted in terms of spectral AOT and A_{ng}, using an algorithm described by *Sano et al.* [2003]. A Glan-Thompson prism was attached in front of the filters to make polarization measurements for retrieving aerosol refractive index. Langley plot calibration measurements were taken at the summit of Mt. Haleakala in Hawaii in February 2001. A second cross-calibration was done in February 2001 at the Shirahama AERONET site in Japan, by direct comparison with a freshly calibrated Cimel CE-318.

Lidar observations were taken at Amami from April 2-7 with a National Institute for Environmental Studies two-channel polarization Lidar; from April 13-26 the Tokyo University of Mercantile Marine Vaisala CT25K ceilometer operated. Cloud screening was performed, using a threshold method, on raw 10 Hz Lidar data that was averaged and recorded every 3 seconds. $\beta_p(532)$ was then derived from the average of all cloud-free profiles in a 15-minute period, using a two-component inversion algorithm [*Fernald*, 1984; *Sugimoto et al.*, 2001]. As part of this procedure, S_a was adjusted so the Lidar-obtained AOT matched the sun photometer value obtained between 0630 and 0700 UTC. The cielometer was designed primarily to detect cloud base, and was calibrated by the manufacturer using a known backscattering material. β_p for free troposphere aerosols, derived from 10-minute averaged ceilometer data, are less accurate than those from the Lidar because of insufficient sensitivity to aerosols over the mixed layer, comparatively wide bandwidth and low energy, and additional attenuation by water-vapor absorption at the ceilometer wavelength. But the data cover a period when the NIES instrument was not operating.

2.15. Regional Meteorology Analysis

Meteorological situations were evaluated using gridded fields from two global models, visible and infared imagery from operational weather satellites, and routine and intensive surface and upper air observations. The NOGAPS model [*Hogan and Rosemond*, 1991] is a global spectral model with a hybrid-sigma vertical coordinate system. The fields used here are at 1° x 1° horizontal resolution, extending from the surface to 150 hPa on isobaric levels, and include the standard thermodynamic and dynamical variables. The vertical resolution in the lower troposphere is high, having eight levels between the surface and 700 hPa (~ 3 km). The data assimilation/forecast cycle produced analysis fields at 0000 and 1200 UTC each day, and short-term forecast fields at 06:00 and 18:00 UTC. We also made use of fields from the NCEP/NCAR Reanalysis archive [*Kalnay et al.*, 1996]. The resolution is lower, 2.5° x 2.5°, but analyzed fields are available four times per day, and a much broader selection of thermodynamic and dynamical variables is available. Further, the same model system has been used for the period from 1957 to the present, allowing unbiased assessment of inter-annual variability. These model results are suitable for diagnostic evaluation of synoptic-scale features, but cloud and precipitation distributions must be estimated using satellite and *in situ* observations. We also made use of air mass trajectory calculations [*HYSPLIT*, 2002] to diagnose the paths of air parcels prior to their arrival in the sampling areas.

3. Environmental Snapshots of Five Multi-Platform Events

This section presents a synthesis of environmental constraints available for the five occasions when MISR took space-based data coincident with two or more participating ACE-Asia surface and airborne platforms (Table 1). All MISR observations occurred between 02:00 and 02:40 UTC. For each event, we review the regional meteorology, air mass history, surface wind, wave, and reflectivity conditions, and available column-integrated as well as layer-by-layer information about spectral *AOT* and particle micro-physical properties. Where similar measurements were taken multiple times in a sampling region, comparisons among these quantities are discussed. Table 3 summarizes the key results at the best-constrained locations for each event. Consensus aerosol optical models are developed in Section 4.

3.1. April 04, 2001 [C-130 + Twin Otter + Ron Brown + Amami Station]

Figure 1A gives a satellite view of a 400 kilometer wide swath extending from just north of Oki Island, in the Japan Sea, to beyond Amami Island in the East China Sea south of Japan, at 02:11 UTC. The locations of four ACE-Asia platforms at overpass time are labeled, and are listed in Table 1.

Regional Meteorology. The C-130 and Twin Otter were nearly co-located in the vicinity of Oki Island, in a cloud-free region filled with dry air having low aerosol loading. They were under the influence of a high-pressure ridge that extended from a surface anticyclone NW of Shanghai on April 2 up to about 4 km, and elongated somewhat as it moved ESE over the subsequent two days. At the time of satellite overpass, the surface pressure exceeded 1012 hPa over the northern part of the study region. West of the study region, a closed anticyclonic circulation was present well above the mixed layer, extending up to 700 hPa.

Back trajectories [*HYSPLIT*, 2002] for the area surrounding Oki Island show that five days previously, the near-surface (500 m) air was located to the NNE, in eastern Mongolia, Manchuria, and the Khabarovsk region of Russia. According to this model, lower tropospheric air (1.5 to 2 km) traveled almost due south across central Siberia and Manchuria, whereas mid-tropospheric air, at 4 to 5 km altitude, came from further west, paralleling the border between Mongolia and Russia where dust sources are common.

The Ron Brown was operating under partial cloud S of Kyushu Island and roughly 670 km S of the aircraft; Amami Island, about 340 km SSW of the Ron Brown, was under total cloud cover. The clouds were part of a frontal band associated with a low pressure center that had formed over NE China, near 45 N, 125 E on April 1, and had moved offshore; at the time of the overpass it was NE of Sakhalin Island.

Frontal passage at the Ron Brown was noted at 0900 UTC on April 03, about 5 hours before overpass time. Back trajectories are similar for the Ron Brown and Amami Island sites, and reflect different history from the Oki air mass. The lower-tropospheric air above these more southerly locations spent the previous five days over a heavily polluted region that includes Korea, the Yellow Sea and the E coast of China. Back trajectories for mid-tropospheric levels are from the east, across open areas of the Pacific Ocean.

Sea Surface Conditions. Near-surface winds around Oki Island are constrained by the air speed - ground speed difference during low-altitude, level flight by the C-130 and Twin Otter. The winds were low, nominally around 3.4 m/s at 54 m elevation for the C-130, and 4.0 m/s at 42 m elevation for the Twin Otter, near satellite overpass time. Visual inspection of the ocean supports the calm sea interpretation; low swell and no whitecaps were observed.

Near-surface winds at the Ron Brown blew consistently from 30° to 50° E of north, at speeds between 10 and 15 m/s, within an hour of the overpass. Wave heights were reported at 2-3 m, consistent with the wind speed, and the surface diffuse reflectance, measured aboard the Ron Brown by the *SIMBAD* radiometer, amounted to 0.0046±0.0003 at 560 nm, diminishing to less than 0.0005 at 670 nm, but augmented by whitecaps. At the Oki site, surface diffuse reflectance is slightly higher, based on analysis of SeaWiFS observations of the region and SIMBAD measurements made near the site on April 13 (Table 3).

Aerosol Properties near Oki Island. In the vicinity of Oki Island, spectral AOT_{col} measured by the *AATS-6* aboard the C-130 and the *AATS-14* on the Twin Otter give a consistent, low-aerosol-optical-depth picture for the region, matching well with the aerosol extinction profiles deduced from the *Neph-130 + PSAP-130* system. For example, on two low-level flight legs, the *AATS-14* $AOT_{col}(525)$ was 0.153, and its spatial variance was around 4%, about the size of the formal measurement uncertainty. The legs lasted 28 minutes, began 32 minutes prior

to the satellite overpass, were constrained to elevations between 30 and 51 m, and covered points separated by as much as 53 km, all near Oki Island. The *AATS-6* $AOT_{col}(526)$ was within 0.142±0.01 over a 15-minute low-level leg, at elevations confined between 47 and 64 m, and covering points separated by 93 km, also near Oki Island. The agreement among these measurements, separated in space and time, speaks to the uniformity of the aerosols in this air mass on scales of tens of kilometers. Since the flight patterns were not designed to uniformly sample an extended area, formal assessment of aerosol air mass variability will be possible with the help of MISR data, once the satellite aerosol retrieval algorithms have been fully validated.

To characterize the total column with a small number of particle types, we define "layers," using minima in the *extinction* vertical profile, elevations marking rapid changes in particle properties, and levels above which the aircraft did not sample well. The lowest ~50-75 m could not be well-observed by the aircraft, but extrapolation to the surface adds negligibly to total column properties in most cases, as can be judged by comparing the *AOT550* uncertainty with the product of the un-sampled near-surface region's thickness and $\sigma_{sp}(550)$ for the lowest layer (Layer 1). ($\sigma_{sp}(550)$ is estimated from the quotient of Layer 1 AOT and Layer 1 vertical extent, given in Table 3 for each case.)

The C-130 flew three vertical profiles, and the TO flew two, within an hour of the MISR overpass; the *AATS*, *Neph-130*, and *OPC-130* data all indicate that below 4.5 km, two aerosol layers were present, within measurement uncertainties (Figure 2). Layer 1 has uniform extinction in a well-mixed column between the surface and about 2.0 km elevation; Layer 2 extends from about 2.0 km to 3.75 km, with peak extinction near 3 km. Along with total-column and layer spectral *AOT*, Table 3 gives a uncertainty estimates that combine systematic measurement uncertainty with observed variability and other random error sources; in this low-variability case, the uncertainty is dominated by systematic terms. Differences between the *AATS-6* and *AATS-14 AOT* produce standard deviations at least an order of magnitude smaller than the measurement uncertainty given. From *AATS*, *AOT(550)* for Layers 1 and 2 amount to 0.084±0.019 and 0.020±0.009, respectively; the corresponding values deduced from in situ measurements with *Neph-130* are in close agreement: 0.079±0.012 and 0.019±0.002.

Several lines of evidence support the idea that a significant fraction of particles in Layer 2 are large, and are probably bright Asian mineral dust, whereas Layer 1 is predominantly smaller, darker, pollution particles. The *AATS* instruments yield ambient $A_{sp}(380,1020)$ of 1.48 in Layer 1, indicating small particles, and 0.48 for Layer 2 (Figure 2, Table 3). In this environment, large particles in an elevated layer are most likely mineral dust, whereas those near the surface may be sea salt. *Neph-130* also identified smaller, darker particles in Layer 1 than aloft, producing of $A_{sp}(550,700)$ for Layer 1 of 1.52±0.40, *SSA(550)* of 0.91±0.02, and a sub-micron fraction *AOT(550)* of 0.77; the corresponding values for Layer 2 are 0.79±0.49, 0.95±0.01, and 0.49±0.06, where the uncertainties are dominated by formal measurement error. These *Neph-130* values are dry; the instrument identified the water contribution to ambient $AOT_{sp}(550)$ as about 15% for Layer 1 and 5% for Layer 2. Having dry particle values from *Neph-130* can account for larger Angstrom exponents than those derived from *AATS*. *Neph-130* also found the large particle fraction increased with height in Layer 1, suggesting these particles may have precipitated from higher elevations, rather than originating at the ocean surface. *OPC-130* and *APS-130* optically effective size distributions (Section 2.3) elaborate on this picture, finding an accumulation mode in Layer 1 having D_c~ 0.3±0.06 microns and σ~ 1.44, along with a weak coarse mode having D_c~ 2.9±0.6 microns, σ~ 2.97, and contributing about 20% to the layer aerosol extinction (Figure 3). The TO sampled only up to 1.8 km within Layer 1, producing an accumulation mode area-weighted peak around 0.24 microns and a weak coarse mode around 1.8 microns. In Layer 2, the C-130 size distributions were somewhat smaller, giving D_c~0.23±0.05 and 2.04±0.41 for the two modes. The upper level coarse mode extinction is similar (though less well-constrained due to lower particle concentration), but the accumulation mode contributes a factor of four or five less than it does to Layer 1.

The *in situ* sampling suite aboard the TO encountered difficulties during the April 04 flight, but *Chem-130* flew legs at three elevations during the two hours subsequent to the satellite overpass (Table 4). Although *OC* and *EC* were not reported for this case, *Chem-130* results support the conclusion that the boundary layer contained significant pollution (high *nss-sulfate*), whereas Layer 2 was enhanced in calcium, a crustal component associated with mineral dust.

Aerosol Properties at the Southern Sites. MPL-RB showed cirrus near 10 km at satellite overpass time, above an aerosol layer confined to the lowest 2 km. Low signal-to-noise

during daylight hours, combined with the boundary and cirrus layer particles, made it difficult to detect any thin, higher-elevation aerosol layers with the Lidar. However, there is the suggestion of very thin aerosol between 2 and 4 km in the data, and after sunset, scattering from a thin layer between 6 and 8 km was detected, though too thin to retrieve *AOT*. For this case, *AOT* data from *Mtps-RB* was not obtained due to cloud contamination.

Although high wind and broken cloud made satellite observations difficult, the Ron Brown site had a well-defined pollution aerosol layer this day similar to the one deduced at the Oki site. *In situ* sampling shows two modes, the first having D_c around 0.28 microns, with a range of about 0.02 to 1.2, and the second at 2 to 3 microns, with a 1 to 10 micron range, all referenced to 55% RH (Figure 4A). The sub-micron particles have 30% to 40% mass fraction *nss-sulfate*, more than 2% *EC*, and a low *SSA(550)* of 0.81 (*Neph-RB*) or 0.86 (*NephRH-RB*), lower than on subsequent days studied here. The super-micron aerosol was composed of 75 to 84% sea salt, with the majority of the remaining mass being dust, producing a *SSA(550)* for the total aerosol of 0.90. *NephRH-RB* humidograph measurements taken of the near-surface aerosols about 2.5 hours before the overpass exhibited deliquescence and hysteresis, showing a difference between $f(RH)_{sp}$ on the upper and lower branches of the hysteresis loop of 33% at *RH* = 70%. Comparing these results with *Neph-RB*, the ambient near-surface aerosols were on the hydrated branch of the hysteresis loop. *NephRH-RB* produced $f(RH)_{sp}$, $A_{sp}(450,550)$, and *SSA* were 1.51, 0.81, and 0.90, respectively, at the ambient *RH* of 63.4%; the low value of A_{sp} may reflect near-surface sea salt.

Further south, the Amami Lidar at satellite overpass time measured a thick cloud layer between 6 and 7 km altitude, in addition to persistent boundary layer cloud at about 1 km, precluding satellite aerosol analysis in this region. The record of photopolarimeter measurements at Amami began about two hours later, giving $AOT_{col}(565)$ around 0.22, and $A_{sp}(443,865)$=0.46, indicating background amounts of large, sea salt particles that are common at the island station.

3.2. April 13, 2001 [C-130 + Twin Otter + Ron Brown]

Figure 1B gives a satellite view from north of Oki Island to about 31°N latitude in the Pacific Ocean just south of Japan, at 02:08 UTC. The locations of three ACE-Asia platforms at the time of overpass are labeled, and are listed in Table 1. The C-130 and Ron Brown were nearly co-located in the vicinity of Oki Island, whereas the Twin Otter flew NE-SW legs near the surface south of Shikoku, about 380 km away, in the Pacific.

Regional Meteorology. The region appears cloud-free, except for broken cumulus over the intervening land. Back trajectories [*HYSPLIT*, 2002] indicate that for the entire experiment region, air at all levels up to 5 km had flowed southeast from central Russia, across east-central Mongolia and the Beijing region of northern China, then over the Yellow Sea and Korean peninsula during the previous five days. An upper-level disturbance that moved offshore from China between 30-40° N latitude strengthened as it passed the Korean peninsula. The mid-latitude storm that it spawned deepened significantly as it moved northeastward from northern Japan on the previous day. The only other significant weather in the vicinity was a weak mid-tropospheric system near Beijing. The ambient humidity was somewhat higher to the west than the east of the sampling region, as a developing anticyclone in the southern part of the area brought increasingly moist air in from southwest of Japan.

Sea surface conditions. Aboard the Ron Brown, the near-surface wind blew consistently from the west, at speeds between 8 and 10 m/s. Whitecaps were noted. A wind speed of 9 m/s was deduced for the C-130 in level flight at about 43 m. Surface diffuse reflectance from *SIMBAD* was 0.007±0.0003 at 550 nm, diminishing to less than 0.001 at 670 nm. Taking into account the effect of whitecaps using a standard, wavelength-independent parameterization [*Monahan and Muircheartaigh*, 1980; *Koepke*, 1984], the total surface albedo is larger, having an estimated value of 0.0085 at 550 nm and 0.0024 at 670 nm. To the south, winds at the Twin Otter were 6±1 m/s at about 40 m altitude, blowing from the WNW.

Aerosol Properties. The atmosphere as viewed from all platforms contained a low-altitude pollution layer and relatively small but spatially uniform total column *AOT*. Dust is a more significant component throughout the column on this day than it was on April 04. For 13 minutes just before the MISR overflight, starting at 01:48 UTC, the C-130 performed a 94-km near-surface leg at 45.5±6 m elevation. During this traverse, *AATS-6* recorded *AOT(526)* 0.246, with a combined variability and measurement uncertainty of ±0.024. Aboard the Ron Brown, *AOT(500)* was reported as 0.30±0.025 over a three-minute period just before the satellite overpass, nominally greater than the mean *AATS-6* value by 0.054. The 45-m elevation difference could contribute only about 0.005, since mid-visible aerosol extinction

was about 0.12 km^{-1} in the surface layer. Using the spectral slope for Layer 1 from Table 3, the RB *AOT(500)* is reduced to 0.288 at 526 nm, just within the 0.230 to 0.292 range in *AOT(526)* observed by *AATS-6* along its traverse, and supporting the spatial variability estimate of <~ 0.02 on 10-km scales deduced from the AATS; the two instruments took data only a few minutes apart, but were separated spatially by 20 to 40 km.

Two vertical profiles, obtained before and after the MISR overpass by the *AATS-6* and the *Neph-130 +PSAP-130*, along with those from the *MPL-RB*, provide a wealth of detail about the column structure (Figure 5). Two layers were identified. According to the *Neph-130 +PSAP-130* and *AATS-6*, the near-surface layer is a mix of fine pollution particles, contributing 0.57±0.07 to $AOT_{sp}(550)$, with coarse sea salt + mineral dust, extending to 1.2 km (Table 3). It represents a total layer *AOT(550)* 0.155, with mean *SSA(550)* 0.92. Ambient $A_{sp}(550)$ from *AATS* comes to 0.78, indicating a greater fraction of large particles in the boundary layer than on April 04, and *SSA(550)* for the sub-micron fraction is about 0.87 from both *Neph-RB* and *Neph-130 +PSAP-130*. This is at least 0.05 higher than at the RB site on April 04, and suggests a lower concentration of boundary layer pollution.

The C-130 optical package and *AATS-6* identified a second layer of dilute pollution between 1.2 and 2.1 km, having a vertical *AOT(550)* 0.044, *SSA(550)* 0.91, and $A_{sp}(550)$ 1.14. The atmosphere between 2.0 and 3.0 km is reported clean, and above this, smaller and somewhat brighter average particles provide an additional 0.065 *AOT(550)* to the column. *Neph-130 + PSAP-130 AOT(550)*, reconstructed for the lower troposphere, agrees to within 0.02 of the *AATS-6* value [*Anderson et al.*, 2003b; *Redemann et al.*, 2003a].

MPL-RB confirms this general structure, finding the well-mixed surface layer up to 1 km, dropping to zero at 2 km, and a weak scattering layer between 3 and 3.5 km. The *MPL* data also indicate a lack of cirrus in the upper troposphere, but show one additional high-altitude aerosol layer, between 7 and 8 km that appears at 0600 UTC, when the signal-to-noise is higher than it is during the satellite overpass.

Chem-RB sampled the near-surface aerosol layer directly. It determined that the sub-micron aerosol fraction was somewhat dustier than on April 04, containing about 15% dust by mass. The super-micron mass fraction was considerably dustier that on April 04, comprising about 60% of the total sample. 10% to 15% of the super-micron mass was identified as sea salt, as might be expected given the ocean surface conditions. Despite the differences in aerosol mixture, the peaks and widths of the area-weighted modal size distributions were very close to those on April 04 (Figure 4). However, the overall near-surface particle number density was higher by about an order of magnitude, due to a nucleation mode having a peak diameter about 0.02 micron, which contributed almost nothing to the area-weighted size distribution.

Chem-130 MOI obtained complimentary data from two samples in the near-surface layer just prior to the MISR overpass (Table 4). Both samples show a moderately polluted air mass having nss-sulfate around 5 $\mu g/m^3$, almost all in the sub-micron fraction. Dust is somewhat more abundant than on April 04, even near the surface, in agreement with the other analyses. The C-130 *OPC* data yields size distributions (Figure 6) showing patterns relative to April 04 (Figure 3) that parallel the differences deduced from *Neph-130+PSAP-130*. D_c in Layer 1 is again about 0.3 microns, and diminishes in Layer 2 to about 0.23 microns. From the combined analysis, as described in Section 2.3, *SSA(550)* in Layer 1 is 0.89±0.04, and is higher, but less-well constrained, in the optically thinner Layer 2, where no coarse mode particles were detected.

A self-consistent analysis of *SeaWiFS* satellite and *SIMBAD* near-surface radiometry (Table 2) was performed [*Li et al.*, 2003]. On April 13, a column-averaged mixture of 57.5% Asian dust (by volume), 35% spherical, non-absorbing, tropospheric particles, and 7.5% soot, was required for the radiative transfer model to agree with both surface and space-based observations over the Ron Brown site. Averaged over the column, this mixture produces *SSA(443)* = 0.834, *SSA(555)* = 0.831, *SSA(670)* = 0.836, and *SSA(865)* = 0.806, lower by 0.07 to 0.1 than the values deduced from the *in situ* measurements. The difference may reflect uncertainties associated with modeling aerosol vertical distribution and rough ocean surface for the remote sensing retrieval on this day.

Single-particle SEM provides yet more detail that is helpful in constraining particle models. Results for a filter sample collected on the Ron Brown between 1:08 and 3:08 UTC show a typical, complex mixture of mineral dust, urban pollution products, and sea salt and its reaction products. Relative number concentrations and mean diameters (microns, in parentheses), for particles having geometric diameters from 0.2 to 20 μm are: silicates having little or no aggregated sulfate, 15.8% (4.9), silicates with aggregated sulfate, 6.1% (3.2), completely reacted sea salt (no Cl remaining), 32.5% (0.9), assorted other sulfates and

nitrates with metal cations, 14.7% (1.3), and iron oxide, 1.2%. About 10% of particles are carbonaceous, having no other detectable elements, though black carbon particles smaller than 0.5 μm are undercounted by the automated analysis method. The remaining particles are primarily complex aggregates of the above types. Black carbon is also aggregated with the above types, with a frequency that will be quantified in future work. The mean dry diameter of the entire sample is 2.1 μm.

For ACE-Asia mineral dust aerosols sampled on several days, particle shape becomes more complex as particle size increases. A simple two-dimensional shape factor, circularity (=perimeter^2/(4π*area)) is calculated from SEM images. Each particle type has its own circularity versus diameter relationship. For particles that do not deliquesce, such as silicates without sulfate, the relationship between average diameter and circularity is approximated by a linear regression line having zero intercept at circularity = 1, and slope 0.12. The approximate circularity of an average 10-μm particle comes to 2.2, less than most other dust-bearing ACE-Asia samples analyzed to date. Such details are included loosely in the optical modeling presented here (Table 5; also *Kalashnikova et al.*, 2003). As further analysis of the ACE-Asia data produces additional constraints on the three-dimensional diversity of particle properties, we may be able to refine the particle micro-physical models using more detail from the IPA data. Consensus optical models for the Oki site on April 13, developed using the same approach used for April 04, are included in Table 6.

The Twin Otter, at the southerly site, did a 21-km, six-minute traverse at 40 m elevation, starting at 01:59 UTC; *AOT(525)* measured by *AATS-14* was tightly constrained to 0.207±0.005. A previous leg, about 17 km to the southwest, had *AOT* about 10% lower. The aircraft flew near-surface for about an hour prior to the satellite overpass, then spiraled up to about 2.2 km. Two layers appear in the *AATS-14* data, one reaching from the surface to 0.7 km, with a peak at 0.5 km, the other extending from about 0.7 to about 1.6 km, with a peak at 1.2 km (Figure 5). The particle size distribution at ambient *RH* in the upper layer is essentially mono-modal, having an area-weighted peak diameter around 0.22 micron at all levels sampled, close to the 0.25- μm -diameter small mode found near Oki. A tail in the upper-layer size distribution, extending to about 7 μm, may hint at a very weak coarse mode. Near the surface, the small mode shows about the same size distribution as in the upper layer, but the super-micron mode is better defined, peaking at about 2.0 micron area-weighted diameter, probably composed of mixed sea salt and dust.

3.3. April 16, 2001 [Twin Otter + Ron Brown + Gosan Station]

Figure 1C gives a satellite view from Jeju Island south to about 31° N latitude, in the Yellow Sea, at 02:17 UTC. The Twin Otter was operating in the vicinity of Gosan Station at this time, under cloud-free conditions; the right side of the nadir-viewing satellite image (Figure 1C) appears murky due to sun glint, not cloud. The Ron Brown was stationed about 200 km to the south, in a region of broken cloud.

Regional Meteorology. The low-level circulation near Gosan was from the south, around a weak center of high pressure centered 470 km to the east. No other regional features directly impacted the meteorology in the study area. At the Ron Brown the humid mixed layer was less than 600 m deep, but grew deeper, and was capped with a layer of dry air up to about 3 km prior to the overpass. Winds from the WSW in the layer from 3 to 5 km driven by a trough to the west over China, brought substantial subtropical moisture, increasing the humidity to near saturation by 03:00 UTC, accounting for the cloudiness.

Back trajectories [*HYSPLIT*, 2002] for the region around Jeju Island indicate air masses having covered the same territory as those for the April 13 study region. Air at all levels up to 5 km flowed southeast from central Russia during the previous five days. The same is true for the Ron Brown site, except that above 3 or 4 km, the air apparently took a more southerly route across central China.

Sea surface conditions. Surface winds at Gosan were reported to come from the SSW at about 6 m/s. The Twin Otter measured winds from the WSW at about 3.5±0.5 m/s during low-level flight around overpass time, at 42±2 m altitude. At the more southerly Ron Brown location, the near-surface wind blew steadily from the ESE, at about 6 m/s, producing light whitecaps and swell of 0.2 m.

Surface diffuse reflectance, measured aboard the Ron Brown by the *SIMBAD* radiometer, amounted to 0.0094±0.0004 at 550 nm, and 0.0016±0.0004 at 670 nm. These numbers are higher than at the Japan Sea and Philippine Sea sites on the previous two overflights,

consistent with our knowledge of ocean color derived from *SeaWiFS* satellite observations. On April 15, *SeaWiFS* imagery covered the southern parts of the Korean Strait and the Yellow Sea, into the north part of the South China Sea (31 to 34 N latitude; 126 to 130 E longitude). The derived marine reflectances were about 0.010, 0.005, and 0.001 at 443, 555, and 670 nm, respectively. They increased slightly to the southwest, but greatly to the northwest, influenced by outflow from the Yangtze and Yellow rivers. At 34N and 126E, values reached 0.04 at 443 and 555 nm, and 0.01 at 670 nm.

Aerosol Properties. Aerosol loading was low this day in the vicinity of Jeju Island, consistent with the air having come from regions that are neither major pollution nor dust sources. The Gosan AERONET sun photometer reported *AOT(500)* of 0.105±0.006, covering the two-hour period centered on the MISR overflight, agreeing, within uncertainties, with *Sun-Gos, Sunphot-Gos,* and with *AOT* calculated from *MPL-Gos*. Also at overpass time, the Twin Otter flew for 26 minutes, 42.6±0.3 m above the surface, along a 70 km leg 100 km SE of Jeju Island. The *AATS-14* recorded $AOT_{col}(525)$ of 0.103±0.007; adjusting to 500 nm using A_{ap} from Table 3, *AOT* is 0.098. At the partly cloudy Ron Brown site, cirrus contributed to making the AOT both much higher and more variable, registering 0.57±0.08 at 500 nm over a nine-minute period about 15 minutes after the overpass.

Vertical profiles around Jeju show two aerosol layers, one having peak concentration 0.5 km above the surface, the other extending from about 1.2 to 2.7 km (Figure 7). The *AATS-14* vertical profile began about 20 minutes after the overpass, about 80 km SE of Gosan Station; it lasted 16 minutes and reached an altitude of 2.5 km. This profile generated a vertical *AOT* for the lower layer of 0.028±0.001 at 550 nm, 0.006±0.001 for the upper layer (to 2.5 km), and 0.055 above. The *MPL-Gos* profile shows similar layering, but the magnitudes of the peaks depend on uncertain interpretation of the data in this case. There is no indication of cirrus in the column from either the *AATS* or *MPL-Gos* profiles, though the steep-slant-path MISR views of the region suggest fairly uniform, sub-visible cirrus over the entire area (Figure 8).

At the more southerly Ron Brown site, cirrus was present at 10 to 12 km at overpass time. *MPL-RB* identified three distinct aerosol layers, one from the surface to 1.0 km, a second between 1 and 2 km, and a third from 2 to 3 km. Here the peak extinction values are higher than at Gosan, about 0.1 km^{-1} in the surface layer, 0.15 km^{-1} in layer 2, and 0.25 km^{-1} in layer 3, all measured at around 01:18 UTC, the closest time to overpass for which data were taken. Over the previous hour, the *AOT* for the upper two layers increased, whereas the near-surface aerosol remained relatively constant, suggesting a possible relationship to the increasing thickness of the humid mixed layer at the time.

Particle size distributions from two teams at Gosan indicate the surface layer was dominated by an accumulation mode having area-weighted dry diameter peaked between 0.2 and 0.3 microns. The corresponding quantity from the Ron Brown was 0.3 μm, but at 55% *RH*; the Twin Otter, at ambient RH and averaged over Layer 1, retrieved 0.24±0.03 microns. A 3-micron coarse mode makes a small additional contribution to the size distribution in the boundary layer at all three sites (e.g., Figure 4C – note the magnified vertical scale, particularly for the super-micron plot). The Twin Otter observed accumulation mode particles in Layer 2 with a size distribution also peaked at 0.24 μm, but no appreciable coarse mode. *Chem-RB* found near-surface particle compositions similar to those on April 13, though in concentrations lower by a factor of two or more. The sub-micron component contained about 20% mass fraction dust or ash, 30% nss-sulfate, and 15% organics, yielding *SSA(550)* around 0.88 at 55% *RH*, whereas the super-micron fraction was dominated by mineral dust, giving a *SSA(550)* around 0.9. *NephRH-RB* measurements between 02:30 and 03:15 UTC show that light scattering and aerosol hygroscopicity were both in the moderate range, with "dry" σ_{sp} = 34.8 Mm^{-1}, σ_{bsp} = 4.3 Mm^{-1}, and $f(RH = 82\%)_{sp}$ = 2.1. Though there was only slight evidence of deliquescence or crystallization, comparison of results from *NephRH-RB* and *Neph-RB* show that the ambient aerosol was again on the hydrated upper branch of the hysteresis loop. *f(RH)*, $A_{sp}(450,550)$, and *SSA(550)* were 2.13, 1.21 and 0.96, respectively, at the ambient *RH* of 84.8%.

Neph-Gos + *PSAP-Gos* found the extinction was evenly divided between the sub- and super-micron modes at the surface. The sub-micron mode had *SSA(550)* of 0.85 and $A_{sp}(450,700)$ of 2.33 at ambient *RH* (72.5%), significantly higher than the dry *SSA* of 0.7. For total aerosol smaller than 10 microns, the *SSA(550)* was 0.90 and $A_{sp}(450,700)$ 1.4 at ambient *RH*, in agreement with values from the Ron Brown. Available total column and layer values, from TO measurements, are given in Table 3.

3.4. April 27, 2001 [C-130 + Twin Otter + Amami Station]

Figure 1D gives a satellite view from the Korean Strait in the north, across Kyushu Island, to Amami Island in the East China Sea, at 02:19 UTC. The Twin Otter was operating in the eastern channel of the Korean Strait, whereas the C-130 performed a circuit across southern Korea that brought it in the vicinity of the Twin Otter early in the flight, from about 01:00 to 02:50 UTC, when it executed a series of east-west legs. Amami Station also appears in the MISR field-of-view, about 620 km south of the aircraft.

Regional Meteorology. All platforms observed a cover of cirrus at satellite overpass time, which may have been formed by divergent flow at the jet stream level. Weak low-level winds and subsidence in the area around Amami were caused by a broad area of high surface pressure, centered over southern Japan and extending east-west about 3000 km. The ridge weakened above 2 or 3 km. A weak low-pressure feature over central China may have produced the area of significant low-level cloudiness just west of the study region.

Back trajectories [*HYSPLIT*, 2002] for the Korean Strait region indicate the air at and above about 4 km had traveled due E over the previous five days, skirting the southern border of Mongolia and crossing the East China Sea south of the Korean Peninsula. Air between 1 and 4 km traveled SE from central Russia, following the Korean coast along the Yellow Sea. Air in the boundary layer traveled nearly due south from the Khabarovsk region of eastern Russia, crossing eastern Manchuria and the Sea of Japan, well east of Korea. The Amami air masses took similar routes, except the lower-level air originated farther west, in eastern Mongolia.

Sea surface conditions. The Twin Otter measured winds from the east of 2±0.5 m/s at 160±20 m elevation, over a 30-minute period that included the satellite overpass. The C-130 also measured low winds, under 1 m/s, at an elevation around 50 m, and the sea surface appeared glassy calm. No near-surface ocean diffuse reflectivity measurements were made in the region, so for modeling purposes, we adopt values measured in the same area on April 04 (Table 3).

Aerosol Properties. AOT from the *AATS* instruments was much more variable than on previous days, most likely due to cirrus contributions. The Twin Otter executed a 34-minute, 52-km east-west traverse just north of latitude 34, starting at 12:51 UTC, and staying between 30 and 40 m above the sea surface. *AATS-14* AOT values behaved systematically during the final 17 minutes of this traverse, but still ranged from about 0.42 to 0.59 at 525 nm, from 0.36 to 0.53 at 675 nm, and from 0.33 to 0.50 at 865 nm. A second traverse, at an altitude of 157±12 m, beginning about 02:27 UTC and lasting 10.5 minutes, produced AOD ranging from 0.52 to 0.72 at 525 nm. The *AATS-6* aboard the C-130 showed similar variability; over the first five minutes of a 28-minute traverse in the area around (34 N, 130 E), starting at 01:22 UTC, AOT at 526 nm stayed within 0.43±0.04, but then jumped to 0.66. During this period, the aircraft remained within 180±19 m above the surface.

There was less variability at the Amami site. For a 50 minute period centered on the satellite overpass, *PSR-Am* measured *AOT(490, 565, 670, 865)* of 0.448±0.014, 0.391±0.016, 0.322± 0.011, and 0.274±0.006, respectively, along with $A_{sp}(443, 865)$ of 1.00.

Although no Lidar was available on any of the platforms this day, the C-130 obtained two vertical profiles over the Korean Strait, the first was completed about 1 hour prior to the MISR overpass and the second began about 20 minutes after the overpass (Figure 9). Here the strength of *in situ* measurements is evident. Horizontal variability in total AOT makes interpretation of the column *AATS* data difficult in this case, but the *Neph-130 + PSAP-130*, along with carefully selected differential optical thickness values from the *AATS*, provide a consistent picture of the aerosol vertical structure (Table 3). These instruments detected a boundary layer up to 1.8 km that contained within it highly concentrated small particles within 200 m of the surface, and aerosols in low concentration in the free troposphere above, based on measurements up to 6.8 km.

The top of the 200 m sub-layer was marked by a sharp *RH* minimum (30-40%), but there was no increase in coarse mode concentration toward the surface, which, along with the low surface wind, makes sea salt particles unlikely. Horizontal variations of ±20% in dry light scattering were observed during level legs flown in the boundary layer at about 500 m between the two profiles. Despite the variability, the boundary layer aerosols appeared to have fairly uniform optical properties (Table 3). Multiple, optically thin layers were observed from the top of the boundary layer to 6.8 km, dominated by coarse-mode, non-hygroscopic aerosol (70% of the scattering), apparently dust. Differences in sampling time, convolved

with horizontal variability, is likely to account for the differences in Layer *AOT* among the instruments.

Size distributions constrained by the TO particle sizers show accumulation mode particles having area-weighted mode diameter of about 0.28±0.04 microns, and a weak coarse mode with diameter around 2.8±0.04 microns near the surface, diminishing to about 2.4±0.04 microns higher up. These results were aggregated from measurements taken at four elevations: 100, 200, 500, and 750 m, all in the lower half of Layer 1 from the profile analysis (Figure 9). *OPC-130* and *APS-130* identify a similar distribution peak for the accumulation mode, up to 1.8 km, but according to these data, the particles are concentrated in two narrow layers, one within a few hundred meters of the surface, and one between about 1.05 and 1.5 km. The coarse mode size distribution is less well defined in these data, particularly above 1 km.

The *Chem-130* analysis adds detail to the boundary layer characterization, based on two legs flown westward at 494 m and eastward at 180 m, respectively, just prior to and during the MISR overpass. Highly polluted air was found: 20 μg OC/m^3 and 3.7 μg EC/m^3 for the upper leg, and 11.7 OC and 2.2 EC in the lower (Table 4). Also, 1.2 μg Ca/m^3 in the samples supports other indications that dust could have dominated the coarse mode. In the upper leg, *OPC-130* found accumulation mode particles with area-weighted size distribution peaking around 0.35 μm, and *APS-130* measured the coarse mode peak to be near 2.5 μm. The Twin Otter flew eastward at 457 m for 30 minutes at about the same time; the particle sizers on board also identified an accumulation mode having area-weighted diameter around 0.28±0.04 μm, and a coarse mode having a broad peak centered near 2.4 μm.

Individual particle analysis was performed on samples from the two C-130 legs at 494 and 180 m elevation just before the overpass. At both elevations, more than 80% of the SEM aerosol particles were dominated by mineral dust and mineral dust aggregates, and the mean dry diameter for all particles 0.2 μm and larger was about 1.55 μm. Black carbon particles having no other detectable elements were < 5% of the 2070 particles larger than 0.2 μm geometric diameter analyzed at both altitudes. Although black carbon particles < 0.5 μm in size were undercounted, these samples show less influence from combustion than the samples analyzed on April 13. These *IPA* results agree qualitatively with the high sub-micron *SSA(550)* obtained by *Neph-130+PSAP-130* in Layer 1, but appear to differ from the exceptionally large boundary layer carbon concentrations measured by *Chem-130*.

For silicates without sulfate, the relationship between mean diameter and circularity can be approximated by a linear regression line having zero intercept at circularity = 1. The corresponding slopes are 0.23 and 0.18 for the 180 m and 494 m samples, respectively, significantly different from the slope of 0.12 for similar particle types in the April 13 sample. These imply an average circularity for 10 μm particles of 3.3 and 2.8, respectively, for the two samples. Having such detail lends confidence to our interpretation of other observation techniques, and makes it possible to develop increasingly accurate component-particle models used in interpreting MISR and other satellite measurements (e.g., Table 5).

3.5. May 02, 2001 [C-130 + Gosan Station]

Figure 1E shows the satellite view of Jeju Island and the south end of the Yellow Sea at 02:39 UTC. The C-130 was operating in a cloud-free region about 85 km SW of Gosan Station at this time. Starting about 02:28 UTC and lasting 1.5 hours, the C-130 flew a series of three stacked, inverted "L"s, to probe atmospheric variability in three dimensions. The base of this pattern ran west 95 km from Gosan over the Yellow Sea toward China, and the stem ran 95 km north from Gosan in the Yellow Sea, parallel to the Korean coast.

Regional Meteorology. Flows in the Jeju region were influenced by a weak, lower-tropospheric cyclonic circulation that had formed in place over SW Japan during the previous 24 hours along a stationary trough of low pressure. The disturbance was confined to levels below 5 km, and the northerly winds on its western side were relatively weak over the Yellow Sea. The clouds over the west side of the Yellow Sea seen in the MISR image are low-level stratus that were dissipating at overflight time.

Back trajectories [*HYSPLIT*, 2002] indicate that the upper level air traveled from central Russia along the northern border of China during the previous few days, roughly as it did on April 13 and 16, and crossed the Yellow Sea to reach Gosan. Air between 2 and 4 km spent the previous five days along the eastern coast of China, in the vicinity of Beijing and Shandong province. Below 2 km, the air came from the east, across the Sea of Japan en route to Gosan.

Sea surface conditions. Near-surface winds of about 3.4 m/s were deduced from the C-130, flying at 39 m at overpass time, over calm seas with no whitecaps. Gosan recorded winds from the E-NE at 6±1 m/s. Since no near-surface ocean diffuse reflectivity measurements were made in the region, for modeling purposes we adopt values measured in the same area on April 16 (Table 3).

Aerosol Properties. The Gosan AERONET sun photometer reported total column AOT 0.319±0.02 at 500 nm, covering the roughly two-hour period centered on the MISR overflight, and an instantaneous value of 0.310 within 10 minutes of the overflight itself, in agreement, within uncertainties, with Sun-Gos and Sunphot-Gos. Sunphot-Gos produced a column-average $A_{ep}(412,862)$ of 1.46±0.02, averaged over two hours around the MISR overpass, compared with 1.37 for AERONET. The C-130 flew 43±3 m above the surface, except during two turns, for about 33 minutes starting at 02:27 UTC. *AATS-6* obtained *AOT(526)* 0.407±0.065 for this entire low-flight period, with extreme values of 0.273 and 0.635. The difference between the C-130 and Gosan values is most likely due to horizontal variability, since the C-130 and Gosan were separated by about 85 km at overpass time; synoptic observations from MISR reinforce this interpretation (Figure 1E).

A three-layer vertical structure was deduced from the C-130's 53-minute ramped descent that started at 6.5 km altitude and reached within 40 m of the surface just before the satellite overpass (Table 3 and Figure 10). The descent was followed immediately by the three stacked "L"s, at 40±3 m, 456±7 m, and 919±11 m, each lasting about 30 minutes. Then a ramped ascent to about 3 km, at the extreme north end of the "L" pattern, was performed. This pattern was aimed at refining *in situ* particle property constraints and at assessing variability.

Aerosols in the vicinity of Jeju Island were characterized by thick, low-level pollution under a relatively aerosol-free upper atmosphere, as might be expected from the trajectory analysis. Surface measurements by *Neph-Gos+PSAP-Gos* determined the sub-micron scattering fraction to be 0.84, *SSA(550)* of 0.95 for sub-10-micron particles, and A_{ep} in the mid-visible as 1.88, all at ambient 78% RH. Aerosol extinction under ambient conditions was 0.245 km^{-1}. These are in close agreement with the averaged Layer 1 results from *AATS-6* and *Neph-130+PSAP-130* (Table 3). Both sets of observations also concluded that over 80% of the scattering was due to moderately hygroscopic, sub-micron particles.

Between 1.3 km and the top of the boundary layer at 2.3 km, the atmosphere was horizontally stratified, devoid of most aerosols, and humid (RH 70 to 100%), with scattered clouds. From 2.3 to 6 km the RH dropped below 20%, and the column remained relatively aerosol-free, producing a total *AOT(550)* of 0.052 from 2.3 km to the top of the atmosphere.

Chem-130 data also identified pollution near the surface, having considerable nss-Sulfate, moderate amounts of OC and EC, and little Ca (Table 4). Above 2.8 km, the aerosol is too sparse to allow good chemical analyses. Qualitatively, chemistry derived from Gosan surface sampling agrees with the *Chem-130* results. For a sample collected between 06:00 UTC on May 02 and 01:00 UTC on May 03, the sub-micron mode is dominated by sulfate, and organic compounds contributed as well; together they account for about 60% of the total mass loading. Very little dust was observed. However, no particle size distribution data are available for this date.

4. Aerosol Optical Models

In Table 6, synthesis aerosol optical models are given for each layer of each event, derived from the layer-by-layer constraints discussed in Section 3. The models are presented as external mixtures of component particles whose properties are listed in Table 5. A "component" is defined as having a single-mode size distribution and uniform composition. The aerosol model for each layer is a mixture of such components. There are three steps in the modeling process. (1) For each event, we used the profile information qualitatively to define layers. (2) For each layer, we then used all available size, composition, and air-mass-source information discussed in Section 3 to help select components and constrain their micro-physical properties. (3) Finally, we mixed the selected components externally as required to quantitatively meet up to six optical constraints for that layer (Table 3), allowing the proportions of each component, and the pollution component *SSA*(550), to vary as needed.

The identities of component aerosols represent the biggest uncertainties in the optical models. They can not be determined uniquely from optical constraints alone; for example, in most cases we could have matched the layer optical constraints with two spherical components, provided we were free to select their size distributions and *SSA*s completely arbitrarily. But we have additional information from *in situ* measurements, which is critical for this study, since we expect MISR to exhibit sensitivity to particle sphereicity and other micro-physical properties [*Kahn et al.*, 2001a], and more generally, because the ability to distinguish anthropogenic from natural aerosols rests on such knowledge.

We began by adopting size distributions specific to each layer as measured on April 04, 13, and 27 by *APS-130* and *OPC-130*, adjusted to ambient *RH*, and those from *DMA-TO* and *APS-TO* for April 16 and 27. Pollution particle models also draw on RB and Gosan Station boundary layer aerosol characterizations. Segregating the size distributions by composition requires additional assumptions (Section 2.3), and was explicitly done only for April 04. So for the purpose of generating optical models to compare with satellite observations, we (1) allow D_c for the pollution component to be either 0.23 or 0.30 microns in Layer 1 (Figures 3, 4, and 6). For Layer 2, only 0.23 micron pollution particles were needed to satisfy available constraints in all cases. (2) We let the pollution component's imaginary index of refraction be a free parameter. Lacking specific information about the state of absorbing material, we in effect treat any black carbon as being internally mixed in the "pollution" component (see, however, the single-particle analysis discussed in Section 3.2). Pollution particles were excluded from the above-the-top layer, but when required to achieve agreement with layer-average optical constraints, (3) we added spherical, non-absorbing "background" components to upper atmospheric layers.

In the absence of information about *SSA* at wavelengths other than 550 nm, we chose indices of refraction independent of wavelength for pollution particles; for dust, we internally mixed clay with 1% hematite by volume [*Sokolik and Toon*, 1999; *Kalashnikova et al.*, 2003]. Pollution, sea salt, and background aerosols were modeled as spherical particles, whereas dust was treated as a mixture of irregular shapes that reproduces the circularity relationships discussed in Sections 3.2 and 3.4 [*Kalashnikova et al.*, 2003].

To decide when to include pollution particle, Asian dust, and sea salt components in a layer, we use as general guides the aircraft-measured chemical abundances (Table 4), RB and Gosan surface sample bulk chemical and *IPA* analyses, air mass trajectories, and available constraints on *SSA* at ambient *RH*. Chemical analyses and back-trajectories also provided qualitative tests of the component mixtures we ultimately derived in each case.

Having selected components, we then solved quantitatively for component fractional abundances separately for each layer, so the calculated values agreed with available layer-average optical constraints to better than the aggregated measurement uncertainty. The optical constraints used (Table 3) are: layer-average $AOT_{ep}(672)$, $AOT_{ep}(558)/AOT_{ep}(672)$, and $AOT_{ep}(866)/AOT_{ep}(672)$ from *AATS* measurements, and layer average sub-micron fraction of $AOT_{ep}(550)$, *SSA(550)*, and sub-micron fraction of *SSA(550)* from *Neph-130 +PSAP-130*, all evaluated at ambient *RH*. For April 16, *SSA* and *RH* constraints come from the *TO* package.

The results from this approach are not unique. They are aimed at producing optical models whose accumulated error, when applied to the analysis of satellite observations, is likely to be less that the sum of formal uncertainties given in Section 2. For example, optical property differences between internal and external component mixtures are unresolved in available measurements. But their impact [e.g., *Conant et al.*, 2003] is probably reduced by constraining layer-average quantities with direct observations. Elevations above Layer 2 (or

for May 02, Layer 3) were sampled remotely, but not directly, by ACE instruments. SAGE II data gives stratospheric $AOT_{ap}(525)$ for the general region as 0.005, and we adopt a standard stratospheric sulfuric acid particle model for this component [*Wang et al.*, 1989; Table 5]. We constrain the aerosol component mixture above the top layer sampled to have spectral *AOT* represented by the difference between the stratospheric *AOT* and the column *AOT* above the top layer, as measured by the *AATS*.

According to Table 6, Layer 1 for all events is modeled primarily with a mixture of pollution particles and accumulation-mode dust, as expected. On April 13, the windiest day, sea salt makes a significant contribution, and on April 16, coarse-mode dust is prominent in the Oki site model, a consequence of a relatively small A_{ap} coupled with an observed lack of sea salt, the other large-sized component used in the modeling. We could also obtain a good fit arbitrarily, with generic "super-micron, non-absorbing spheres." But we limited the number of components as much as possible, and generic spheres are not invoked in Layer 1.

Overall agreement among models and observations is well within measurement uncertainties; Table 7 shows the differences between the model and measurements for each constraint, along with the sizes of the corresponding measurement uncertainties.

Except on April 27, smaller sub-micron fractions of *AOT(550)* correspond to lower A_{ap} in the boundary layer (Table 3), a consistent indication of larger particles from both sun photometer and nephelometer measurements. But simultaneously meeting constraints on the sub-micron fraction of *AOT(550)*, the sub-micron *SSA(550)*, and the total aerosol *SSA(550)* places tight restrictions on component properties and abundance. For example, on April 13 and 16, sub-micron *SSA(550)* is low, 0.85 and 0.87, respectively, and the sub-micron fraction of *AOT(550)* is close to 0.6 on both days. This means the larger particles must have *SSA(550)* near the physical limit of unity, if the total *SSA(550)* is to reach the reported values of 0.90 and 0.92 (Table 3). The super-micron components identified by *Chem-RB* and other observations (mineral dust, and for April 13, sea salt as well), have the required high *SSA* values, and the model adopts sub-micron pollution particles having *SSA(550)* of 0.80±0.01 for these cases. On April 04 and May 02, sub-micron *AOT* fraction and *SSA* are both high in Layer 1, so the models contain brighter pollution particles (*SSA(550)*=0.90±0.02) and small super-micron fraction in the dust accumulation mode.

The in situ measurements appear to give differing results on April 27 – *Neph-130+PSAP-130* report a relatively high *SSA(550)* for both sub-micron and all particles in Layer 1 (Table 3), whereas *Chem-130* finds both OC and EC abundance at two levels in the boundary layer to be dramatically higher for this event than any other in our sample (Table 4). In addition, the sub-micron fraction of *AOT(550)* is not as high as might be expected given the high A_{ap} value, suggesting particle size distributions different from those on other days, though results from both the C-130 and Twin Otter particle sizing instruments do not support this conclusion (see Section 3.4), though chemical analysis from near-coincident Twin Otter measurements also show high carbon values [*Mader et al.*, 2002]. The model adopts a modest amount of coarse dust, along with a large fraction of pollution particles, to reproduce the two quantities. Sampling differences are likely responsible for the apparent measurement discrepancies, since higher horizontal and vertical variability were noted on this day than on others, and we do not have enough information to justify creating additional component particles for this event.

The *AOT* for Layer 2 is two-to-four times lower than for Layer 1 (except on May 02, when it is almost 20 times lower), even though the second layer is still within 2.5 km of the surface on all but April 04 and 27. Sampling is more difficult when particle concentrations are low, and optical determinations of aerosol properties are close to uncertainty levels in some cases (Table 3). As expected, we can again produce models that meet the constraints from a mix of dust and pollution, with the addition of cirrus on April 27, when Layer 2 extends to almost 7 km, and small particles on April 16, a case for which the sub-micron *AOT(550)* fraction and A_{ap} are both exceedingly high (Table 3). Model results are well within the measurement uncertainties for all events (Table 7).

Only spectral optical depths are used to constrain the aerosol models above the top layer. These constraints are easily met with mixtures of medium spherical non-absorbing particles, accumulation mode dust, and the assumed stratospheric sulfate component. For April 27, we include a small amount of cirrus, which helps reproduce the low value of A_{ap} (Table 3), and reflects the cirrus observed in the study region on that day.

5. Conclusions

Detailed, multi-platform field measurements taken as part of the ACE-Asia campaign constrain to within a few percent the optical properties of atmosphere and surface on five occasions, while the MISR instrument aboard the EOS Terra satellite made column-integrated observations from space. We developed optical models based on a synthesis of field observations, representing environmental snapshots of a range of clean, polluted, and dusty aerosol conditions. The results, summarized in Tables 3, 5, and 6, are aimed at two broad categories of satellite studies: vicarious low-light-level radiometric calibration, and aerosol retrieval validation. For radiometric calibration, top-of-atmosphere radiances can be calculated from the surface and atmospheric constraints developed here, and compared directly with radiances measured by the satellite instrument. For aerosol validation, we can use the MISR research retrieval to determine ranges of aerosol mixtures, components, and amounts that produce simulated MISR radiance values that agree with those observed for each event, to within measurement uncertainty [e.g., *Kahn et al.*, 2001a].

We obtained vertical profiles of optical data for all five events (Figures 2, 5, 7, 9, and 10), and defined layers based on changes with height of sampling, aerosol amount, or aerosol type. Our optical models amount to event- and layer-specific mixtures of component particles. We derived component particle characteristics from the height-resolved particle size and bulk composition information collected. Ambiguities remain in segregating the size distributions by composition. For the purpose of satellite aerosol validation, and for many other aerosol radiative impact studies, the segregation process is equivalent to assigning spectral *SSA* values to each component. In this experiment, particle *SSA* was measured only at 550 nm; having simultaneous measurements at one or two additional wavelengths would go a long way toward closing the remaining gaps in environmental characterization for these applications.

To determine aerosol mixtures for each atmospheric layer, we selected components based upon the aggregate of available *in situ* chemical and physical observations, along with meteorological context. We then solved quantitatively for component particle abundance, constrained by up to six event-specific, layer-average optical parameter measurements, which are presented together with their uncertainties in Tables 3 and 7. The results of this process are not unique, but they provide a means of constraining, with field measurements taken at a variety of scales, optical models useful for satellite inter-comparison studies.

As expected, aerosols within a few kilometers of the surface during the ACE-Asia study were composed primarily of pollution and Asian dust mixtures. For one event, April 13, high surface wind added sea salt to the column, and on another, April 27, cirrus was present, along with greater horizontal spatial variability than on other days. To the degree they were constrained, accumulation and coarse-mode particle size distributions varied little among the events studied. However, column *AOT* changed by more than a factor of four, the proportion of dust in the lowest atmospheric layer ranged from about 25% (April 27) to 50% (April 16, just after the peak of a major dust event), and the amount of absorbing material in the sub-micron fraction varied considerably. For modeling purposes, we assumed the absorbing material was internally mixed in the "pollution" component; *SSA(550)* for this component was around 0.8 on April 13 and 16, when the near-surface wind crossed Beijing and the Korean Peninsula. For the other events, days when near-surface air originated in eastern Mongolia (April 04) or eastern Korea and the Japan sea (April 27 and May 02), this quantity was close to 0.9.

For layers above 1 or 2 km, *AOT* was considerably smaller, and observations were less constraining of the models. Among the upper-layer models, an interesting result was obtained for April 16, when 22% of a very small, non-absorbing component was required to match observations, though we could not identify any unique environmental factor to link with this component. Spectral optical depth measurements, the only constraints available above the highest levels directly sampled by aircraft, were easily fit, though not uniquely, with mixtures of Asian dust and accumulation-mode non-absorbing spheres. Up-welling spectral flux measurements, especially at the top of the column sampled by aircraft, and down-welling near-surface flux measurements were unavailable for this study, but could provide valuable integral constraints on such models.

In addition to creating environmental snapshots, one conclusion of this study is insight into the complementary nature of surface, *in situ*, and satellite aerosol observations. Surface and aircraft remote sensing, nephelometer, and *PSAP* data produced layer-average optical constraints upon which vertical aerosol structure models were built. For the MISR validation cases, we relied on a cascade of more detailed physical and chemical aerosol measurements,

down to *IPA*, to gain confidence in particle size distributions, shapes, and composition, all of which are needed under ambient conditions to create an accurate optical description of the column. Taken together, these measurements provide details about height-resolved particle micro-physical properties which can not be retrieved from any current or anticipated satellite data alone.

But once MISR aerosol retrieval algorithms are validated, and the quantitative limitations of the measurements assessed, coincident satellite data can fill in the regional aerosol picture, identifying gradients in aerosol amount and column-averaged properties, and quantifying variability in two dimensions. The similarities in component size distribution and chemical identity among the events studied here suggest that even in this relatively complex aerosol environment, detailed component particle micro-physical properties derived from a subset of cases can be applied more generally. A considerable body of literature supports the idea that aerosol types exhibit seasonal and spatial patterns that repeat from year to year, and that micro-physical properties of broad classes of mineral dusts, sea salt, biomass burning, pollution, and background particles vary little for many of the largest sources. If satellite observations can map the extent of aerosol air mass types [e.g., *Kahn et al.*, 2001a], and targeted *in situ* measurements provide adequate constraints on component properties, we can obtain a detailed global picture of aerosol behavior.

Follow-on work to the present study is needed to evaluate the relationship between variability observed in one [e.g., *Anderson et al.*, 2003a; b] and two dimensions, which will help establish practical limits as to how closely satellite and *in situ* data sets can be combined. Additional effort at applying spatial statistical methods to formally combining aerosol observations taken at multiple spatial [e.g., *Huang et al.*, 2002] and temporal scales would be valuable for this effort as well. Having such results in hand would provide a strong scientific basis for suggesting coordinated surface, *in situ*, and satellite measurement strategies needed to meet global aerosol monitoring requirements in the future.

Acknowledgements

We thank our many ACE-Asia colleagues for their support of this effort, including the ACE-Asia project staff, flight teams, ground teams, and funding agencies. The Joint Office of Science Support (JOSS), under the University Corporation for Atmospheric Research (UCAR) provided major logistical support for the United States portion of this effort. The work of R. Kahn is supported in part by the Climate and Radiation Research and Analysis Program in the Earth Sciences Division of the National Aeronautics and Space Administration, under D. Anderson, the National Oceanographic and Atmospheric Administration Office of Global Programs under J. Levy, and the NASA EOS-MISR instrument program. His work is performed at the Jet Propulsion Laboratory, California Institute of Technology, under contract with NASA. The MISR effort was also assisted by the MISR Team, including David Diner, Barbara Gaitley, Earl Hansen, Duncan McDonald , John Martonchik, and Kyle Miller. This research is a contribution to the International Global Atmospheric Chemistry (IGAC) Core Project of the International Geosphere Biosphere Program (IGBP) and is part of the IGAC Aerosol Characterization Experiments (ACE).

References

Allan, J., J. Jimenez, P. Williams, M. R. Alfarra, K. N. Bower, J. T. Jayne, H. Coe, D. Worsnop, Quantitative sampling using an Aerodyne aerosol mass spectrometer. Part 1: Techniques of data interpretation and error analysis. *J. Geophys. Res.*, 108, #4090, 2003.

Anderson, J.R., P.R. Buseck, T.L. Patterson, and R. Arimoto, Characterization of the Bermuda tropospheric aerosol by combined individual-particle and bulk-aerosol analysis, *Atmos. Environ.* 30, 319-338, 1996.

Anderson, T. L. and J.A. Ogren, Determining aerosol radiative properties using the TSI 3563 integrating nephelometer, *Aerosol Sci. Technol.* 29, 57-69, 1998.

Anderson, T. L., R.L. Charlson, D.M. Winker, J.A. Ogren, and K. Holmen, Mesoscale variations of tropospheric aerosols, *J. Geophys. Res.* 60, 119-136, 2003a.

Anderson, T. L., Masonis, S. J., Covert, D. S., Ahlquist, N. C., Howell, S. G., Clarke, A. D., and McNaughton, C. S., Variability of aerosol optical properties derived from in-situ aircraft measurements during ACE-Asia, *J. Geophys. Res.*, submitted, 2003b.

Bates, T.S., P. K. Quinn, D. J. Coffman, J. E. Johnson, T. L. Miller, D. S. Covert, A. Wiedensohler, S. Leinert, A. Nowak, and C. Neususs, Regional physical and chemical properties of the marine boundary layer aerosol across the Atlantic during Aerosols 99: An overview, *J. Geophys. Res. 106,* 20,767, 2001.

Bates, T.S., P.K.Quinn, D.J. Coffman, D.S. Covert, T.L.Miller, J.E. Johnson, G.R. Carmichael, S.A. Guazzotti, D.A. Sodeman, K.A. Prather, M. Rivera, L.M. Russell, and J.T. Merrill, Marine boundary layer dust and pollution transport associated with the passage of a frontal system over eastern Asia, *J. Geophys. Res.*, submitted, 2003.

Berner, A., C. H. Lurzer, F. Pohl, O. Preining and P. Wagner, The size distributions of urban aerosols in Vienna, *Sci. Total Environ.* 13, 245-261, 1979.

Bond, T. C., Anderson, T. L. and Campbell, D., Calibration and intercomparison of filter-based measurements of visible light absorption by aerosols, *Aerosol Sci. Technol.* 30, 582-600, 1999.

Brechtel, F. J., S. M. Kreidenweis, and H. B. Swan, Air Mass Characteristics, Total Particle Concentration and Size Distributions at Macquarie Island, Tasmania, During the First Aerosol Characterization Experiment (ACE 1). *J. Geophys. Res.* 103, 16,351-16,367, 1998.

Brechtel, F.J., and S. M. Kreidenweis, Predicting Particle Critical Supersaturation from Hygroscopic Growth Measurements In the Humidified TDMA. Part II: Laboratory and Ambient Studies. *J. Atmosph. Sci.* 57, 1872-1887, 2000.

Brock, C. A., M. Trainer, T. B. Ryerson, J. A. Neuman, D. Parish, J. Holloway, D. Nicks, Jr., G. Frost, G. Hubler, F. Fehsenfeld, J.C. Wilson, J. M. Reeves, B. G. Lalfleur, H. Hilbert, E. Atlas, S. Donnelly, and S. Schauffler. Particle Growth in Urban and Industrial Plumes in Texas, *J. Geophys. Res.* 108, D3, #4111, 2003.

Buzorius, G., A. Zelenyuk, F. Brechtel, and D. Imre, Simultaneous Observations of Single Particle Size, Hygroscopicity and Chemical Composition by Coupled HTDMA-Mass Spectrometry. *Geophys. Res. Lett.* 29, #1947, 2002.

Campbell, J.R., D.L. Hlavka, E.J. Welton, C.J. Flynn, D.D. Turner, J.D. Spinhirne, V.S. Scott, and I.H. Hwang, "Full-time, Eye-Safe Cloud and Aerosol Lidar Observation at Atmospheric Radiation Measurement Program Sites: Instrument and Data Processing", *J. Atmos. Oceanic Technol.*, 19, 431-442, 2002.

Carrico, C.M., Kus, P., Rood, M.J., Quinn, P.K., and Bates, T.S., Mixtures of pollution, dust, seasalt and volcanic aerosol during ACE-Asia: Aerosol Radiative properties as a function of relative humidity, Submitted to *J. Geophys. Res.*, in press, 2003.

Clarke, A.D., A thermo-optic technique for in situ analysis of size-resolved aerosol physicochemistry, *Atmos. Env.* 25A, 635-644, 1991.

Clarke, A. D., S. Howell, P. K. Quinn, T.S. Bates, E. Andrews, A. Jefferson, J. A. Ogren, A. Massling, O. Mayo-Bracero, H. Maring, D. Savoie, G. Cass The INDOEX aerosol: A comparison and summary of microphysical, chemical, and optical properties observed from land, ship, and aircraft, *J. Geophys. Res.* 107, #8033, 2002.

Collins, D.R., R.C. Flagan, and J.H. Seinfeld, Improved inversion of scanning DMA data, *Aerosol. Sci. Technol. 36(1)*, 1-9, 2002.

Conant, W.C., J.H. Seinfeld, J. Wang, G.R. Carmichael, Y. Tang, I. Uno, P.J. Flatau, K.M. Markowicz, P.K. Quinn, A model for the radiative forcing during ACE-Asia derived from CIRPAS Twin Otter and R/V Ronald H. Brown data and comparison with observations, Submitted to *J. Geophys. Res.*, 108, #8661, 2003.

Delene, D.J. and J.A. Ogren, Variability of aerosol optical properties at four North American surface monitoring sites, *J. Atmos. Sci.* 59, 1135-1150, 2001.

Deschamps, P.-Y., B. Fougnie, R. Frouin, P. Lecomte, and C. Verwaerde, SIMBAD: A field radiometer for satellite ocean color validation. *Appl. Optics*, submitted, 2002.

Diner, D.J., J.C. Beckert, T.H. Reilly, C.J. Bruegge, J.E. Conel, R. Kahn, J.V. Martonchik, Ackerman, T.P., R. Davies, S.A.W. Gerstl, H.R. Gordon, J-P. Muller, R. Myneni, R.J. Sellers, B. Pinty, and M.M. Verstraete, Multiangle Imaging SpectroRadiometer (MISR) description and experiment overview, *IEEE Trans. Geosci. Remt. Sensing 36*, 1072-1087, 1998.

Diner, D.J. W.A. Abdou, J.E. Conel, K.A. Crean, B.J. Gaitley, M.Helmlinger, R.A. Kahn, J.V. Martonchik, and S.H. Pilorz, MISR aerosol retrievals over southern Africa during the SAFARI-2000 dry season campaign, *Geophys. Res. Lett.* 28, 3127-3130, 2001.

Doherty, S., Anderson, T. L. and Charlson, R. J., Measurement of the lidar ratio for atmospheric aerosols using a 180°-backscatter nephelometer, *Appl. Optics* 38, 1823-1832, 1999.

Dubovik, O. and M. D. King: A flexible inversion algorithm for retrieval of aerosol optical properties from Sun and sky radiance measurements," *J. Geophys. Res.* 105, 20 673-20 696, 2000.

Dubovik, O., A. Smirnov, B. N. Holben, M. D. King, Y.J. Kaufman, T. F. Eck, and I. Slutsker: Accuracy assessments of aerosol optical properties retrieved from AERONET sun and sky-radiance measurements, *J. Geophys. Res.* 105, 9791-9806, 2000.

Dutton, E.G. and J.R. Christy: Solar radiative forcing at selected locations and evidence for global lower tropospheric cooling following the eruptions of El Chichón and Pinatubo. *Geophys. Res. Lett.* 19, 2313-2316, 1992.

Dutton, E.G., P. Reddy, S. Ryan, and J.J. DeLuisi,, Features and effects of aerosol optical depth observed at Mauna Loa, Hawaii: 1982-1992. *J. Geophys. Res.* 99, 8295-8306, 1994.

Dutton , E.G., J..J. Michalasky, T. Stoffel, B.W. Forgan, J. Hickey, D.W. Nelson, T.L. Alberta, and I. Reda,: Measurement of broadband diffuse sollar irradiance using current commercial instrumentation with a correction for thermal offset errors. *J. Atmos. Oceanic Tech.* 18, 297-314, 2001.

Dutton, E.G. and B.A. Bodhaine, Solar irradiance anomalies caused by clear-sky transmission variations above Mauna Loa 1957-1999. *J. Clim.* 14, 3255-3262, 2001.

Eck, T.F., B.N.Holben, J.S.Reid, O.Dubovik, A.Smirnov, N.T.O'Neill, I.Slutsker, and S.Kinne: Wavelength dependence of the optical depth of biomass burning, urban and desert dust aerosols, *J. Geophys. Res.* 104, 31 333-31 350, 1999.

Fernald, F. G., Analysis of atmospheric lidar observations: Some comments, *Appl. Opt.* 23, 659-653, 1984.

Fougnie, B., R. Frouin, P. Lecomte, and P.-Y. Deschamps, 1999: Reduction of skylight reflection effects in the above-water measurement of marine diffuse reflectance. *Appl. Optics* 38, 3844-3856, 1999.

Hogan, T. F. and T. E. Rosemond, "The description of the US Navy Operational Global Atmospheric Prediction System's spectral forecast model," *Mon. Wea. Rev.* 119, 1786-1815, 1991.

Holben B.N., T.F.Eck, I.Slutsker, D.Tanre, J.P.Buis, A.Setzer, E.Vermote, J.A.Reagan, Y.Kaufman, T.Nakajima, F.Lavenu, I.Jankowiak, and A.Smirnov, "AERONET - A federated instrument network and data archive for aerosol characterization", *Rem. Sens. Environ.* 66, 1-16, 1998.

Huang, H-C, N. Cressie, and J. Gabrosek, Fast, resolution-consistent spatial prediction of global processes from satellite data, J. Comput. & Graph. Statictics 11, 63-88, 2002.

Huebert, B.J., T. Bates, P.B. Russell, G. Shi, Y.J. Kim, K. Kawamura, G. Carmichael and T. Nakajima, An overview of ACE-Asia: strategies for quantifying the relationships between Asian aerosols and their climatic impacts, accepted, *J. Geophys. Res*, 2003a.

Huebert, B.J., T. Bates, P.B. Russell, G. Shi, Y.J. Kim, K. Kawamura, G. Carmichael and T. Nakajima, An overview of ACE-Asia: Technical Appendix, accepted, *J. Geophys. Res*, 2003b.

Huebert, B., T. Bertram, S. Howell, D. Eatough, J. Kline, and B. Blomquist, Measurements of Organic and Elemental Carbon in Asian Outflow During ACE-Asia from the NSF/NCAR C-130, to be submitted *J. Geophys. Res.* 2003c.

HYSPLIT (Hybrid Single-Particle Lagrangian Integrated Trajectory) Model, 2002. Web address: http://www.arl.noaa.gov/ready/hysplit4.html, NOAA Air Resources Laboratory, Silver Spring, MD.

Jayne, J.T., D.C. Leard, X.F. Zhang, P. Davidovits, K.A. Smith, C.E. Kolb, and D.R. Worsnop, Development of an aerosol mass spectrometer for size and composition analysis of submicron particles, *Aerosol Sci. and Tech.* 33 (1-2), 49-70, 2000.

Kahn, R., P. Banerjee, and D. McDonald, The Sensitivity of Multiangle Imaging to Natural Mixtures of Aerosols Over Ocean , *J. Geophys. Res. 106*, 18219-18238, 2001a.

Kahn, R., P. Banerjee, D. McDonald, and J. Martonchik, Aerosol Properties Derived from Aircraft Multi-angle Imaging Over Monterey Bay, *J. Geophys. Res. 106*, 11977-11995, 2001b.

Kahn, R., P. Banerjee, D. McDonald, and D. Diner, Sensitivity of Multiangle Imaging to Aerosol Optical Depth, and to Pure-Particle Size Distribution and Composition Over Ocean , *J. Geophys. Res. 103*, 32,195-32,213, 1998.

Kalashnikova, O.V., R. Kahn, and I.N. Sokolik, The ability of multi-angle remote sensing observations to identify and distinguish dust CCS types: Part 1. Theoretical Framework, J. Geophys. Res., in preparation, 2003.

Kalnay, E., M. Kanamitsu, R. Kistler, W. Collins, D. Deaven, L. Gandin, S. Saha, G. White, J. Woollen, Y. Zhu, M. Chelliah, W. Ebisuzaki, W.Higgins, J. Janowiak, K. C. Mo, C. Ropelewski, J. Wang, A. Leetmaa, R. Reynolds, R. Jenne, and D. Joseph, "The NCEP/NCAR 40-Year Reanalysis Project," *Bull. Amer. Meteor. Soc.*, 77, 437-471, 1996.

Kasten, R., Visibility in the prephase of condensation, *Tellus* 21, 631-635, 1969.

Klett, D., Stable analytical inversion solution for processing lidar returns, *Appl. Opt.* 20, 211-220, 1981.

Koepke, P., Effective reflectance of oceanic whitecaps, Appl. Opt. 23, 1816-1824, 1984.

Lafleur, B. G. A Low Turbulence Inlet for Airborne Aerosol Sampling, MSME Thesis, University of Denver, Denver, CO, 1998.

Lee, K.H., Hee S. Jung, Young J. Kim, Chang H. Jung, Size Calibration Correction for a HAYCO OPC from Different Aerosol Models. July 2002 Progress Report, Kwangju Institute of Science and Technology.

Li, L-P., H. Fukushima, R. Frouin, B.G. Mitchell, M-X. He, I. Uno, T. Takamura, and S. Ohta, Imfluence of sub-micron absorptive aerosol on SeaWiFS-derived marine reflectance during ACE-Asia, *J. Geophys. Res. 108*, D15, #4472, 2003.

Liu, Z, N. Sugimoto, and T. Murayama: Extinction-to-backscatter ratio of Asian dust observed by high-spectral-resolution lidar and Raman lidar, accepted for publication in *Appl. Opt.* 41, 2760-2767, 2002.

Livingston J. M., P. B. Russell, J. S. Reid, J. Redemann, B. Schmid, D. A. Allen, O. Torres, R. C. Levy, L. A. Remer, B. N. Holben, A. Smirnov, O. Dubovik, E. J. Welton, J. R. Campbell, J. Wang, S. A. Christopher, Airborne sunphotometer measurements of aerosol optical depth and columnar water vapor during the Puerto Rico Dust Experiment, and comparison with land, aircraft, and satellite measurements, *J. Geophys. Res.*, 108 (D19): #8588, doi:10.1029/2002JD002520, 2003.

Mader B.T., R.C. Flagan , and J.H. Seinfeld, Airborne measurements of atmospheric carbonaceous aerosols during ACE-Asia, *J. Geophys. Res.*, 107 (D23): #4704, 2002.

Martonchik, J.V., D.J. Diner, R. Kahn, M.M. Verstraete, B. Pinty, H.R. Gordon, and T.P. Ackerman, Techniques for the Retrieval of aerosol properties over land and ocean using multiangle imaging, IEEE Trans. Geosci. Remt. Sensing 36, 1212-1227, 1998.

Miller, M. A., K. Knobelspiesse, R. Frouin, C. Pietras, M. J. Bartholomew, R. M. Reynolds, E. J. Welton, G. Fargion, and P. K. Quinn, "Shipboard Measurements of Atmospheric Radiation and Aerosol Optical Properties during ACE-Asia", *J. Geophys. Res.* ***, 2003.

Monahan, E.C., and I.O. Muircheartaigh, Optimal power-law description of oceanic whitecap coverage dependence on wind speed, *J. Phys. Oceanogr.* 10, 2094-2099, 1980.

Murayama, T. et al., Ground-based network observation of Asian Dust events of April 1998 in east Asian, *J. Geophys. Res.* 106, 18345-18359, 2001.

Ohmura, A., E.G. Dutton, and 13 co-authors. Baseline Surface Radiation Network (BSRN)/WCRP), a new precision radiometry for climate research. *Bull. Amer. Meteoro. Soc.*79, 2115- 2136, 1998.

Quinn, P.K., D.J. Coffman, T.S. Bates, T.L. Miller, J.E. Johnson, K. Voss, E.J. Welton, and C. Neusüss, Dominant aerosol chemical components and their contribution to extinction during the Aerosols99 cruise across the Atlantic, *J. Geophys. Res. 106*, 20,783, 2001.

Quinn, P.K., D.J. Coffman, T.S. Bates, T.L. Miller, J.E. Johnson, E.J. Welton, C. Neusüss, M. Miller, and P. Sheridan, Aerosol optical properties during INDOEX 1999: Means, variabilities, and controlling factors, *J. Geophys. Res. 107, (D19) #8020*, 2002.

Redemann, J., S. J. Masonis, B. Schmid, T. L. Anderson, P. B. Russell, J. M. Livingston, O. Dubovik, and A. D. Clarke, Clear-column closure studies of aerosols and water vapor aboard the NCAR C-130 during ACE-Asia, 2001, *J. Geophys. Res. 108,* (D23), 8655, doi:10.1029/2003JD003442, 2003a.

Redemann, J., B. Schmid, J.A. Eilers, R. Kahn, R.C. Levy, P.B. Russell, J.M. Livingston, P.V. Hobbs, W.L. Smith Jr., B.N. Holben, Suborbital measurements of spectral aerosol optical depth and its variability at sub-satellite-grid scales in support of CLAMS, 2001, *J. Geophys. Res.*, submitted, 2003b.

Remer, L.A., Tanré, D., Kaufman, Y.J., Ichoku, C., Mattoo, S., Levy, R., Chu, D.A., Holben, B.N., Martins, J.V., Li, R.R., & Ahmad, Z., Validation of MODIS Aerosol Retrieval Over Ocean, *Geophysical Research Letters 29*, 1618, 2002.

Russell, P. B., J. M. Livingston, P. Hignett, S. Kinne, J. Wong, and P. V. Hobbs, Aerosol-induced radiative flux changes off the United States Mid-Atlantic coast: Comparison of values calculated from sunphotometer and in situ data with those measured by airborne pyranometer, *J. Geophys. Res., 104*, 2,289-2,307, 1999.

Russell, P. B., J. M. Livingston, E. G. Dutton, R. F. Pueschel, J. A. Reagan, T. E. DeFoor, M. A. Box, D. Allen, P. Pilewskie, B. M. Herman, S. A. Kinne, and D. J. Hofmann, Pinatubo and pre-Pinatubo optical-depth spectra: Mauna Loa measurements, comparisons, inferred particle size distributions, radiative effects, and relationship to lidar data, *J. Geophys. Res., 98*, 22,969-22,985, 1993.

Sano I., S. Mukai, Y. Okada, B. N. Holben, and T. Takamura, Retrieval of aerosol properties during APEX and ACE-Asia experiments, *J. Geophys. Res.* 108, 8649, 2003.

Schmid B., D. A. Hegg, J. Wang, D. Bates, J. Redemann, P. B. Russell, J. M. Livingston, H. H. Jonsson, E. J. Welton, J. H. Seinfeld, R. C. Flagan, D. S. Covert, O. Dubovik, and A. Jefferson. Column closure studies of lower tropospheric aerosol and water vapor during ACE-Asia using airborne sunphotometer, airborne in-situ and ship-based lidar measurements. *J. Geophys. Res., 108*(D23), 8656, doi:10.1029/2002JD003361, 2003a.

Schmid B., J. Redemann, P. B. Russell, P. V. Hobbs, D. L. Hlavka, M. J. McGill, B. N. Holben, E. J. Welton, J. R. Campbell, O. Torres, R. A. Kahn, D. J. Diner, M. C. Helmlinger, D. A. Chu, C. Robles Gonzalez, and G. de Leeuw, Coordinated airborne, spaceborne, and ground-based measurements of massive, thick aerosol layers during the dry season in southern Africa, *J. Geophys. Res*, 108(D13), 8496, doi:10.1029/2002JD002297, 2003b.

Schmid, B., J. M. Livingston, P. B. Russell, P. A. Durkee, H. H. Jonsson, D. R. Collins, R. C. Flagan, J. H. Seinfeld, S. Gassó, D. A. Hegg, E. Öström, K. J. Noone, E. J. Welton, K. Voss, H. R. Gordon, P. Formenti, and M. O. Andreae, Clear sky closure studies of lower tropospheric aerosol and water vapor during ACE-2 using airborne sunphotometer, airborne in-situ, space-borne, and ground-based measurements, *Tellus, 52B*, 568-593, 2000.

Sheridan, P.J., D. J. Delene and J.A. Ogren, Four years of continuous surface measurements from the Department of Energy's Atmospheric Radiation Measurement Program Southern Great Plains Cloud and Radiation Testbed site, *J. Geophys. Res. 106*, 20735-20747, 2001.

Smirnov A., B.N.Holben, T.F.Eck, O.Dubovik, and I.Slutsker, Cloud screening and quality control algorithms for the AERONET data base, *Rem.Sens.Env.* 73, 337-349, 2000.

Sokolik, I.N., and O.B. Toon, Incorporation of mineralogical composition into models of the radiative properties of mineral aerosol from UV to IR wavelengths, *J. Geophys. Res.* 104, 9423-9444, 1999.

Spinhirne, J. D., Compact eye safe lidar systems, *Rev. Laser Eng.* 23, 112-118, 1995.

Spinhirne, J. D., J. Rall, and V. S. Scott, "Compact eye-safe lidar systems", *Rev. Laser Eng.* 23, 26-32, 1995.

Sugimoto, N., I. Matsui, Z. Liu, A. Shimizu, K. Asai, K. Yoneyama and M. Katsumata: Latitudinal distribution of aerosols and clouds in the western Pacific observed with a lidar on board the research vessel Mirai, *Geophys. Res. Lett. 28*, 4187-4190, 2001.

Tang, I. N., and H. R. Munkelwitz, Simultaneous determination of refractive index and density of evaporating solution droplets, *Aerosol Science and Technology 15*, 201-207, 1991.

Wang, P-H, M.P. McCormick, T.J. Swissler, M.T. Osborn, W.H. Fuller, and G.K. Yue, Inference of stratospheric aerosol composition and size distribution from SAGE II satellite measurements, *J. Geophys. Res. 94*, 8435-8446, 1989.

Wang, J. et al., Clear-column radiative closure during ACE-Asia: Comparison of multi-wavelength extinction derived from particle size and composition with results from sun photometry, *J. Geophys. Res.107*, (D23), #4688, 2002.

Wang, J., R. C. Flagan, and J.H. Seinfeld. A differential mobility analyzer (DMA) system for submicron aerosol measurements at ambient relative humidity, *Aerosol. Sci. Technol.* 37 (1), 46-52, 2003.

Welton, E. J., K. J. Voss, H. R. Gordon, H. Maring, A. Smirnov, B. Holben, B. Schmid, J. M. Livingston, P. B. Russell, P. A. Durkee, P. Formenti, and M. O. Andreae, "Ground-based Lidar Measurements of Aerosols During ACE-2: Instrument Description, Results, and Comparisons with other Ground-based and Airborne Measurements", *Tellus*, 52B, 635-650, 2000.

Welton, E. J., J. R. Campbell, J. D. Spinhirne, and V. S. Scott, Global monitoring of clouds and aerosols using a network of micro-pulse lidar systems, in Lidar Remote Sensing for Industry and Environmental Monitoring, U. N. Singh, T. Itabe, N. Sugimoto, (eds.), *Proc. SPIE, 4153*, 151-158, 2001.

Welton, E.J., K.J. Voss, P.K. Quinn, P.J. Flatau, K. Markowicz, J.R. Campbell, J.D. Spinhirne, H.R. Gordon, and J.E. Johnson, "Measurements of aerosol vertical profiles and optical properties during INDOEX 1999 using micro-pulse lidars", *J. Geophys. Res.* 107, (D19), #8019, 2002.

Welton, E.J., and J.R. Campbell, "Micro-pulse Lidar Signals: Uncertainty Analysis", *J. Atmos. Oceanic Technol.*, 19 (12), 2089-2094, 2002.

Willeke, K and P. A. Baron, Aerosol Measurement: principles, techniques, and applications. Van Nostrand Reinhold, 876pp, 1993.

Yoon, S. C. and J. G. Won, Monitoring of atmospheric aerosols in Seoul using a micro pulse lidar, in 19th International Laser Radar Conference, NASA/CP-1998-207671 /PT1, PP.83-85, 1998.

Zelenyuk, A., and Imre, D., A new single-particle laser-ablation time-of-flight mass spectrometer for size-resolved composition measurements of ambient particulate matter. Paper presented at the annual meeting of the American Association for Aerosol Research, Portland, OR, 2001.

Figure Captions

Figure 1. MISR true-color images for the five overpass events, with the locations of the ACE-Asia study platforms indicated. (A) April 04, 2001, Terra Orbit 6884, Path 112, MISR Blocks 61-68, nadir view. (B) April 13, 2001, Terra Orbit 7015, Path 111, MISR Blocks 62-65, 26° aft view. (C) April 16, 2001, Terra Orbit 7059, Path 116, MISR Blocks 64-65, 26° aft view. (D) April 27, 2001, Terra Orbit 7219, Path 113, MISR Blocks 63-68, nadir view. (E) May 02, 2001, Terra Orbit 7292, Path 116, MISR Block 64, nadir view.

Figure 2. Vertical profiles from the Twin Otter *AATS-14*, the C-130 *AATS-6*, and *Neph-130 + PSAP-130* instruments for April 04, 2001. The left panel shows aerosol extinction as a function of height, the middle panel presents $A_{ap}(380, 1020)$. At right are three panels showing spectral optical depth for the entire column (bottom), Layer 1 (middle), and Layer 2(top). C-130 data are averages of three profile flights that began at 00:02, 00:54, and 1:54 UTC, and lasted about 40 minutes each. The two profiles contributing to the TO observations began at 0:10 and 1:25 UTC. The symbols and plots are color coded according to the source data: red for *AATS-6*, blue for *AATS-14*, and green for *Neph-130+PSAP-130*.

Figure 3. Vertical structure of area-weighted aerosol optically effective size distribution, adjusted to ambient *RH* (Section 2.3) for April 04, 2001, 1:53 to 2:32 UTC, from *OPC-130* and *APS-130*.

Figure 4. Aerosol area-weighted size distributions at 55% *RH* and particle number densities in the boundary layer, derived from *DMPS-RB*, *APS-RB*, and *CPC-RB*, as described in Section 2.7. (A) April 04, 2001. (B) April 13, 2001. (C) April 16, 2001. Vertical red lines help identify the relative locations of the size distribution peaks for the three Events.

Figure 5. Same as Figure 2 for April 13, 2001. C-130 data are averages of two profiles that began at 00:16 and 01:05 UTC, the first lasting about 15 minutes, the second, about 47 minutes.

Figure 6. Vertical structure of area-weighted aerosol optically effective size distribution, adjusted to ambient *RH*, for April 13, 2001, 2:05 to 2:30 UTC, from *OPC-130* and *APS-130*.

Figure 7. Same as Figure 2 for April 16, 2001. Twin Otter *AATS-14* data are averages of two profiles that began at 00:04 and 01:33 UTC, and lasted 24 and 28 minutes, respectively.

Figure 8. MISR true-color nadir image for April 16, 2001, Terra Orbit 7059, Path 116, MISR Blocks 64-65, 70° forward view, processed the same as Figure 1C for comparison.

Figure 9. Same as Figure 2 for April 27, 2001. C-130 *AATS-6* and *Neph-130 +PSAP-130* data are taken from two profiles that began at 01:03 and 2:36 UTC.

Figure 10. Same as Figure 2 for May 02, 2001. C-130 *AATS-6* and *Neph-130+PSAP-130* data taken during the ramped descent that began at 01:46 UTC, covering a 104-km region around 33 N latitude, 126 E longitude, East of Jeju Island.

Table 1. MISR Multi-Platform Coincident Events During the ACE-Asia Campaign †

• April 04, 2001 Oki and Amami Islands

MISR Orbit **6884**, Path 112, 02:14:12 UTC at Block 61
C130 flight RF03 (Block 61) – Best AATS: 1:52:48 UTC [36.28 N, 132.95 E] Elev. 54 m, Oki
Twin Otter flight RF03 (Block 61) – [36.497 N, 133.33 E] Elevation 41.93 m, Sea of Japan
RV Ron Brown Day 94 (Block 66) – [30.66 N, 131.50 E] Philippine Sea
Amami Surface Station (Block 68) – [28.44 N, 129.70 E]

• April 13, 2001 Oki Island

MISR Orbit **7015**; Path 111, 02:08:14 UTC at Block 62
C130 flight RF08 (Block 62) – Best AATS: 1:59:24 UTC [35.78 N, 132.58 E] Elev. 45 m
Twin Otter flight RF08 (Block 65) -- [32.37 N, 132.59 E] Elevation 41.12 m
RV Ron Brown Day 103 (Block 62) – [35.74 N, 132.50 E]

• April 16, 2001 Gosan Station, Jeju Island

MISR Orbit **7059**; Path 116, 02:16:37 UTC at Block 64
Twin Otter flight RF10 (Block 64) -- [32.85 N, 127.14 E] Elev. 41.92 m, in Local Mode area
RV Ron Brown Day 106 (Block 65) – [31.20 N, 126.31 E] in MISR swath, south of Local Mode
Gosan Surface Station (Block 64) – [33.28 N, 126.17 E]

• April 27, 2001 Oki and Amami Island

MISR Orbit **7219**, Path 113, 02:20:47 UTC at Block 63
C130 flight RF15 (Block 63) -- circuit across southern Korea and back through the Sea of Japan,
coincident data taken Best AATS: 02:36:40 UTC [34.00 N, 130.30 E] Elev. 52 m
Twin Otter flight RF17 (Block 63) - Best AATS: 2:21:30 UTC [34.03 N, 129.49 E] Elev. 165m
Amami Surface Station (Block 68) – [28.44 N, 129.70 E]

• May 02, 2001 Gosan Station, Jeju Island

MISR Orbit **7292**, Path 116, 02:39:30 UTC at Block 64
C130 flight RF18 (Block 64) – Best AATS: 02:36:00 UTC [33.08 N, 125.38 E] Elev. 39 m
Gosan Surface Station (Block 64) – [33.28 N, 126.17 E]

† Times are rounded to the nearest minute, and locations to the nearest hundredth of a degree. The MISR Overpass lasts 7.5 minutes, because a given east-west line of real estate comes into view for each of the nine push-broom cameras, successively, over this period, beginning with the 70° forward view. The nominal time given is the mid-point of the sequence over the primary target. For the C-130, "Best AATS" positions are reported, since this instrument had a short integration time. MISR times report when the nadir camera reached the MISR Block indicated.

Table 2. Measurements Included in this Study

Acronym	Name	Institution	Measured/Derived Quantities
Terra Satellite			
MISR	Multi-angle Imaging SpectroRadiometer	Jet Propulsion Laboratory	Top-of-atmosphere reflectance at 9 view angles x 4 wavelengths (446, 558, 672, 867 nm) for a 400-km swath, of 0.275 to 1.1 km pixels; interpreted as column aerosol optical depth and particle type
C-130			
Neph-130	Integrating Nephelometers (five)	U. Washington Seattle	σ_{sp}, b, $A_{sp}(550,700)$, for all particles and for sub-micron particles at 450, 550, and 700 nm, at <45% RH; and for 540 nm also at 85% RH, plus β_p at 532 nm and <45% RH; all with about 30 sec sampling
PSAP-130	Particle Soot Absorption Photometers (two)	U. Washington Seattle	σ_{ap} at 550 nm and <45% RH, for all particles and for sub-micron particles; combined with Neph-130 to give *SSA*
OPC-130	Optical Particle Counter	U. Hawaii	Particle size distribution from 120 nm to 15 μm, every 30 seconds on ascent and descent; 30 seconds each on unheated, 150°C, 300°C for level legs
APS-130	Aerosol Particle Spectrometer	U. Hawaii	Particle size distribution from 0.8 to 12 μm, every 30 seconds
Chem-130	Aerosol Particle Samplers (three)	U. Hawaii	*OC* and *EC* from PC-BOSS sampler, Bulk inorganic chemical composition from TAS, and composition for super- and sub-micron size ranges from MOI
SEM/TEM	Scanning & Transmission Electron Microscopes	Arizona State U.	Inorganic particle composition, size, and shape, along with fine-scale structure and mixing states for particles down to 10 nm
AATS-6	Ames Airborne Tracking Sunphotometer	NASA/Ames Research Center	*AOT* at five wavelengths from 380 to 1021 nm, A_{ep}, water vapor extinction, and water vapor density profiles, about every 4 seconds.
Twin Otter			
AATS-14	Ames Airborne Tracking Sunphotometer	NASA/Ames Research Center	*AOT* at 13 wavelengths from 354 to 1558 nm, A_{ep}, water vapor extinction, and water vapor density profiles, about every 4 seconds.
DMA-TO	Differential Mobility Analyzers (two)	Cal. Tech.	Size distribution from 15 nm to 1 μm diameter every 100 sec, at dry and ambient RH
APS-TO	Aerodynamic Particle Sizer	Cal. Tech.	Size distribution from 0.5 to 20 μm in aerodynamic diameter at ambient RH every 20 seconds.
R/V Ron Brown			
Mtps-RB	Microtops sun	NOAA PMEL	AOT at 380, 440, 500, 675, and 870 nm

	photometer		
CPC-RB	Condensation Particle Counter	NOAA PMEL & U. Washington	Total particle number concentration for particles having diameters > 3 nm, every minute
DMPS-RB	Differential Mobility Particle Sizer	NOAA PMEL & U. Washington	Aerosol size distribution in 27 bins between 22 and 900 nm diameter, every 15 minutes
APS-RB	Aerodynamic Particle Sizer	NOAA PMEL & U. Washington	Aerosol size distribution between 0.6 and 9.6 μm aerodynamic diameter, every 15 minutes
Neph-RB	Integrating Nephelometer	NOAA PMEL	σ_{sp} at 450, 550, and 700 nm and 55% RH, every minute
PSAP-RB	Particle Soot Absorption Photometer	NOAA PMEL	σ_{ap} at 565 nm and 55% RH, every minute
Chem-RB	Aerosol Particle Sampler	NOAA PMEL	Sub- and super-micron aerosol component mass fractions; dust, sea salt, nss-Ca, nss-Mg, EC, organic matter (POM), H_2O, NH_4, NO_3
NephRH-RB	Scanning RH integrating nephelometers	U. Illinois	σ_{sp} and σ_{bsp} at 450, 550, and 700 nm, for particle diameters < 10 μm and < 1 μm (alternating), scanning 35% < RH < 85%; one sample per hour
MPL-RB	Micro-Pulse LIDAR	NASA/GSFC	Vertical structure of aerosol and cloud from one-channel (523 nm) backscatter, at 1-minute time and 75-m height resolution
SIMBAD	Hand-held SIMBAD Radiometer	Scripps Institution of Oceanography	AOT at 443, 490, 560, 670, and 870 nm and Diffuse Marine Reflectance at 443, 490, 560, and 670 nm
Gosan Station			
AERONET	CIMEL Sun Photometer	NASA/GSFC	AOT at 340, 380, 440, 500, 670, 870, and 1020 nm, every 15 min; hourly particle size distribution, phase function, and *SSA*
MPL-Gos	Micro-Pulse LIDAR	Seoul National U.	Vertical structure of aerosol and cloud from one-channel (523 nm) backscatter, at 10-minute time and 30-m height resolution
DMA-Gos	Differential Mobility Analyzer	Brookhaven National Laboratory	Dry size distribution from 0.005 to 0.6 μm diameter once per minute
OPC-Gos	Optical Particle Counters (two)	KMA/METRI and NOAA/ UCSC/ BNL	Dry particle size distribution from 0.3 to 25 μm diameter every 10 minutes
HTDMA-Gos	Humidified Tandem Differential Mobility Analyzer	Brookhaven National Laboratory	Size-resolved hygroscopic growth for dry particle diameters between 0.02 and 0.3 μm at controlled RH values, integrated over a few hours on each of eight separate days
AMS-Gos	Aerodyne Mass Spectrometer	UMIST	30-minute time series averaged loadings, and chemical size distributions of sulfate, nitrate, and organic components for particles in the diameter range 0.03 to 2.0 μm
Sun-Gos	Sun photometer	KMA/METRI	AOT at 368, 500, 675, 778, and 862 nm, once per minute

Met-Gos	Meteorology station	Korea Meteorological Administration	Temperature, relative humidity, wind, and atmospheric pressure at 10 m elevation, once per minute
Sunphot-Gos	Carter-Scott sun photometers (two)	CMDL	AOT at 368, 410, 500, 610, 675, and 862 nm, every minute
Neph-Gos	TSI nephelometers (two)	CMDL	σ_{sp} at 450, 550 and 700 nm as a function of scattering angle and RH, for sub-micron and sub-10 micron particles, every minute
PSAP-Gos	Particle Soot Absorption Photometer	CMDL	σ_{ap} at 565 nm; combined with Neph, single SSA for sub-micron and sub-10 micron particles, every minute
Amami Station			
Ceil-Am	ceilometer	Tokyo U. of Mercantile Marine	Cloud base heights and backscattering profile by aerosol and cloud at 905nm up to 7.5km with 15-sec time and 15-m height resolutions
Lidar-Am	NIE Compact Mie Lidar	NIES	Backscattering profile (532 nm, 1064 nm) and depolarization ratio profile (532 nm) at 10-sec time and 30-m height resolution
PSR-Am	Sun photo-polarimeter	Kinki U.	AOT at 443, 490, 565, 670, 765, and 865 nm every minute

Table 3. Aerosol and Surface Property Constraints for Key Multi-Platform Cases †

Date	April 04	April 13	April 16	April 27	May 02
Site/ Platform	Oki C-130 / TO	Oki C-130 / RB	Gosan TO	Oki C-130 / TO	Gosan C-130
Thumb-nail Description	Calm surface, low AOT, low AOT variability	High wind, modest AOT, low AOT variability, some dust, near-surface sea salt	Calm surface, low AOT	Calm surface, modest AOT, BL pollution, dust aloft, AOT variable, scattered cirrus	Calm surface, modest AOT, mainly BL pollution, scattered cloud at BL top
Surface Winds (m/s)	3 to 4	8 to 10	3 to 4	1 to 2	3 to 5
Surface Diffuse Reflectivity	0.007 (550) <0.001 (670)	~0.0085 (550) ~0.0024 (670) (includes whitecaps)	~0.009 (550) ~0.0016 (670)	0.007 (550) <0.001 (670) (best guess)	~0.009 (550) ~0.0016 (670) (best guess)
Column Aerosol *AOT**	0.245±0.017 (380) 0.200±0.015 (446) 0.154±0.014 (550) 0.152±0.014 (558) 0.121±0.013 (672) 0.090±0.012 (866) 0.075±0.012 (1021)	0.358±0.025 (380) 0.304±0.024 (446) 0.247±0.024 (550) 0.243±0.024 (558) 0.202±0.023 (672) 0.156±0.023 (866) 0.132±0.023 (1021)	0.143±0.011 (380) 0.116±0.008 (446) 0.090±0.006 (550) 0.089±0.006 (558) 0.073±0.005 (672) 0.057±0.004 (866) 0.050±0.004 (1021)	0.699±0.027 (380) 0.598±0.026 (446) 0.486±0.026 (550) 0.479±0.026 (558) 0.399±0.025 (672) 0.311±0.025 (866) 0.264±0.024 (1021)	0.595±0.026 (380) 0.468±0.026 (446) 0.341±0.025 (550) 0.334±0.025 (558) 0.252±0.025 (672) 0.172±0.024 (866) 0.134±0.024 (1021)
sub-micron fraction $AOT_{ep}(550)$#	0.80±0.04	0.69±0.05	--	0.66±0.05	0.83±0.05
A_{ep}(380,1020)	1.20	1.01	1.07	0.98	1.51
SSA (550)#	0.94±0.02	0.93±0.02	--	0.93±0.02	0.94±0.02
Layer 1:					
Extent (km)	0.075 to 2.0	0.074 to 1.2	0.042 to 1.0	0.106 to 1.8	0.044 to 1.3
Layer 1 AOT_{ep}	0.147±0.026 (380) 0.115±0.023 (446) 0.084±0.019 (550) 0.083±0.019 (558) 0.063±0.017 (672) 0.045±0.017 (866)	0.186±0.018 (380) 0.164±0.017 (446) 0.139±0.017 (550) 0.138±0.017 (558) 0.119±0.017 (672) 0.098±0.016 (866)	0.047±0.001 (380) 0.037±0.001 (446) 0.028±0.001 (550) 0.027±0.001 (558) 0.022±0.001 (672) 0.017±0.001 (866)	0.486±0.022 (380) 0.368±0.021 (446) 0.255±0.020 (550) 0.248±0.020 (558) 0.179±0.019 (672) 0.115±0.017 (866)	0.494±0.082 (380) 0.384±0.069 (446) 0.276±0.055 (550) 0.270±0.054 (558) 0.202±0.044 (672) 0.136±0.033 (866)

	0.036±0.013 (1021)	0.086±0.016 (1021)	0.015±0.000 (1021)	0.086±0.016 (1021)	0.105±0.028 (1021)
AOT(550) Neph-130	0.079±0.012	0.155±0.026	--	0.335±0.043	0.254±0.054
sub-micron fraction $AOT_{ep}(550)$	0.77±0.05	0.57±0.07	0.60	0.65±0.05	0.85±0.04
$A_{ep}(380,1020)$	1.43	0.78	1.13	1.75	1.57
SSA (550)	0.91±0.02	0.92±0.02	0.90	0.92±0.02	0.93±0.02
SSA(550) sub-micron	not measured	0.87±0.03	0.85	0.91±0.02	0.93±0.02
RH_{ave}	43%	55%	57%	41%	74%
RH_{max}	70%	75%	--	86%	88%
water fraction $AOT_{ep}(550)$	0.15±0.10	0.16±0.11	--	0.09±0.05	0.32±0.26
Layer 2:					
Extent (km)	2.0 to 3.75	1.2 to 2.1	1.0 to 2.54	1.8 to 6.94	1.3 to 2.3
Layer 2 AOT_{ep}	0.026±0.009 (380) 0.023±0.009 (446) 0.020±0.009 (550) 0.020±0.009 (558) 0.018±0.009 (672) 0.016±0.008 (866) 0.014±0.008 (1021)	0.063±0.018 (380) 0.052±0.017 (446) 0.041±0.017 (550) 0.040±0.017 (558) 0.033±0.017 (672) 0.024±0.016 (866) 0.020±0.016 (1021)	0.020±0.002 (380) 0.012±0.002 (446) 0.006±0.001 (550) 0.006±0.001 (558) 0.004±0.001 (672) 0.002±0.001 (866) 0.002±0.001 (1021)	0.109±0.114 (380) 0.111±0.094 (446) 0.114±0.073 (550) 0.114±0.072 (558) 0.116±0.057 (672) 0.119±0.042 (866) 0.121±0.034 (1021)	0.022±0.026 (380) 0.018±0.025 (446) 0.014±0.023 (550) 0.014±0.023 (558) 0.011±0.021 (672) 0.009±0.019 (866) 0.007±0.018 (1021)
AOT(550) Neph-130	0.019±0.002	0.044±0.005	--	0.076±0.011	0.020±0.004
sub-micron fraction $AOT_{ep}(550)$	0.49±0.06	0.70±0.05	0.85	0.28±0.04	0.65±0.09
$A_{ep}(380,1020)$	0.62	1.14	2.53	-0.11	1.12
SSA (550)	0.95±0.01	0.91±0.02	--	0.94±0.01	0.95±0.01
SSA(550) sub-micron	not measured	0.89±0.02	--	0.85±0.03	0.94±0.02
RH_{ave}	14%	32%	5.6%	9%	74%
RH_{max}	39%	28%	7.0%	37%	100% (cloud)
water	0.05±0.02	0.11±0.06	--	0.02±0.01	0.39±0.29

fraction $AOT_{ep}(550)$					
Layer 3:					
Extent (km)	--	--	--	--	2.3 to 5.48
Layer 3 AOT_{ep}	--	--	--	--	0.037±0.025 (380) 0.032±0.025 (446) 0.026±0.024 (550) 0.026±0.024 (558) 0.021±0.024 (672) 0.017±0.023 (866) 0.014±0.023 (1021)
AOT(550) Neph-130	--	--	--	--	0.017±0.002
sub-micron fraction $AOT_{ep}(550)$	--	--	--	--	0.63±0.05
A_{ep}(380,1020)	--	--	--	--	1.69
SSA (550)		--	--	--	0.92±0.01
SSA(550) sub-micron	--	--	--	--	0.89±0.02
RH_{ave}	--	--	--	--	9%
RH_{max}	--	--	--	--	59%
water fraction $AOT_{ep}(550)$	--	--	--	--	0.03±0.02
Above the Top Layer Sampled[#]:					
AOT_{ep}	0.072±0.016 (380) 0.061±0.015 (446) 0.049±0.014 (550) 0.048±0.013 (558) 0.039±0.013 (672) 0.029±0.012 (866) 0.024±0.012 (1021)	0.110±0.025 (380) 0.087±0.024 (446) 0.065±0.024 (550) 0.063±0.024 (558) 0.049±0.024 (672) 0.034±0.023 (866) 0.027±0.023 (1021)	0.079±0.010 (380) 0.067±0.007 (446) 0.055±0.005 (550) 0.054±0.005 (558) 0.046±0.003 (672) 0.037±0.003 (866) 0.033±0.002 (1021)	0.130±0.026 (380) 0.115±0.026 (446) 0.097±0.026 (550) 0.096±0.026 (558) 0.083±0.025 (672) 0.068±0.025 (866) 0.060±0.024 (1021)	0.037±0.025 (380) 0.032±0.025 (446) 0.026±0.024 (550) 0.026±0.024 (558) 0.021±0.024 (672) 0.017±0.023 (866) 0.014±0.023 (1021)
A_{ep}(380,1020)	1.10	1.44	0.89	0.79	0.95

† Entries in this table are best-estimate values under ambient conditions; see text for details. The following abbreviations are used: TO=Twin Otter; RB= Research Vessel Ron Brown. Wavelength (in nm) is given in parentheses where needed. Water fraction $AOT_{ep}(550)$ is the difference between *AOT* at ambient RH and at 30% RH, as deduced from *Neph-130*. The multi-spectral *AOT* numbers reported are as follows: April 04 – the average of *AATS-6* on the C-130 and AATS-14 on the TO; April 13, April 27, May 02 – *AATS-6* only; April 16 – *AATS-14* only. Due to highly variable cirrus on April 27, the *AATS-6* observations for Layer 1 were obtained from the profile that began at 2:36 UTC, for Layer 2, from the 1:03 UTC profile, and the above-the-top-layer observations from the transit profile at 3:13 UTC. For all other cases, the profiles used are the same as those in the corresponding profile plots.
* Uncertainties given for *Neph-130+PSAP-130* observations are the formal measurement error [*Anderson et al.*, 2003]. Additional uncertainty arises due to ambient variation, as discussed in the text. For the total-column *AATS* data, these are assessed based on short-distance horizontal variability, and combined as the root-sum-square with the formal measurement error, which amounts to assuming the two contributions are independent. For the *AATS-14* layer AOT, only the horizontal variability term is retained, since formal measurement errors should cancel between layer top and bottom. For *AATS-6* layer data, horizontal variability and half the formal measurement error are combined, to account for pointing uncertainty with that instrument [see *Redemann et al.*, 2003].
# For the above-the-top layer, we assume the unmeasured $SSA(550) = 0.98$ and sub-micron fraction $AOT_{ep}(550) = 0.98$, as additional constraints to produce total-column quantities.

Table 4. Chem-130 Analyses Near Satellite Overpass Times †

Date	Start (UTC)	Stop (UTC)	Alt Range (km)	nss-Sulfate ($\mu g/m^3$)	NH_4 ($\mu g/m^3$)	NO3 ($\mu g/m^3$)	Soluble Ca ($\mu g/m^3$)	OC ($\mu g/m^3$)	EC ($\mu g/m^3$)
April 04	02:49	03:12	3.18-2.67	3.1 ± 0.6	1.1 ± 0.7	1.9 ±0.8	1.9 ± 0.9	--	--
April 04	03:16	03:45	2.30-1.16	5.5 ± 0.5	2.1 ± 0.6	1.9 ±0.6	1.2 ± 0.7	--	--
April 04	03:49	04:14	0.049-0.628	8.1 ± 0.6	2.9 ± 0.6	1.9 ±0.7	1.2 ± 0.8	--	--
April 13	01:16	01:45	0.616-1.27	4.9	--	1.0	2.4	4.3 ±1.2	1.2 ± 0.6
April 13	01:48	02:06	0.032-0.187	5.0	--	1.5	2.1	4.8 ±1.6	2.1 ± 0.9
April 27	01:36	02:03	0.470	--	--	--	--	20.2 ± 2.4	3.7 ± 0.9
April 27	02:06	02:35	0.190	--	--	--	--	11.7 ± 1.7	2.5 ± 0.6
May 02	02:28	03:02	0.044-0.255	8.9± 0.5	3.6± 0.4	2.3± 0.4	1.2± 0.5	8.1 ±1.3	1.5± 0.6
May 02	03:06	03:34	0.456-0.496	8.4± 0.5	3.4± 0.5	1.8± 0.5	0.3± 0.6	7.0± 1.4	1.2± 0.7
May 02	03:37	04:08	0.935-0.921	4.9± 0.4	2.0± 0.5	1.7± 0.5	0.4± 0.6	5.1± 1.1	1.1± 0.6
May 02	04:31	05:07	2.836-2.853	--	--	--	--	1.3± 0.7	1.3± 0.7
May 02	05:30	06:18	0.247-0.261	11.4± 0.6	3.4± 0.3	3.7± 0.3	0.6± 0.4	5.2± 0.9	1.3± 0.5

† Values without error bars are from *MOI*, all others are from *TAS*.

Table 5. Representative Component Aerosol Models*

Component Name	D1 (μm)	D2 (μm)	Dc (μm)	σ	nr	ni	Sub-μm Fract. AOT (550)	SSA (558)	SSA (672)	SSA (866)	s_{ep} (558)	s_{ep} (672)	s_{ep} (866)	g	Particle Size/Shape Category
Pollution_0.23_ssa-0.77	0.005	10	0.23 area	1.48	1.47	0.04	1.000	0.769	0.732	0.659	0.025	0.017	0.009	0.573	Medium Spherical
Pollution_0.23_ssa-0.82	0.005	10	0.23 area	1.48	1.47	0.03	1.000	0.817	0.785	0.721	0.024	0.016	0.009	0.573	Medium Spherical
Pollution_0.30_ssa-0.83	0.005	10	0.30 area	1.6	1.47	0.035	0.992	0.826	0.811	0.777	0.063	0.046	0.028	0.672	Medium Spherical
Pollution_0.23_ssa-0.87	0.005	10	0.23 area	1.48	1.47	0.02	1.000	0.871	0.847	0.796	0.023	0.015	0.008	0.572	Medium Spherical
Pollution_0.30_ssa-0.89	0.005	10	0.30 area	1.44	1.47	0.02	0.999	0.891	0.877	0.844	0.069	0.048	0.026	0.645	Medium Spherical
Pollution_0.23_ssa-0.91	0.005	10	0.23 area	1.48	1.47	0.014	1.000	0.906	0.888	0.848	0.023	0.015	0.007	0.571	Medium Spherical
Pollution_0.30_ssa-0.92	0.005	10	0.30 area	1.44	1.47	0.014	0.999	0.922	0.911	0.886	0.069	0.047	0.025	0.643	Medium Spherical
Sphere_0.05_ssa-1.0	0.005	0.3	0.05 area	1.48	1.43	0	1.000	1	1	1	4.9E-06	2E-06	8E-07	0.053	Medium Spherical
Sphere_0.3_ssa-1.0	0.05	2	0.3 area	1.48	1.43	0	1.000	1	1	1	0.056	0.038	0.020	0.654	Medium Spherical
Sphere_0.5_ssa-1.0	0.05	2	0.5 area	1.48	1.43	0	1.000	1	1	1	0.351	0.276	0.180	0.742	Medium Spherical
Asia_Accum_Dust_Grains	0.2	2	1.0 num.	1.5	1.51	0.0011 (672); 7.12 E-4 (865)	0.407	0.977	0.991	0.995	2.881	3.082	3.106	0.673	Medium Non-spherical
Asia_Coarse_Dust	0.2	12	2.0 num.	2	1.51	0.0011 (672); 7.12 E-4 (865)	0.081	0.897	0.949	0.975	2.354	3.363	2.605	0.661	Large Non-spherical
Sea Salt	0.05	15	3.3 area	3.02	1.48	0	0.231	1	1	1	1.735	1.758	1.783	0.739	Large Spherical

High_Alt _Sulfate	0.05	10	0.90 num.	1.3	1.43	0	0.819	1	1	1	2.429	2.616	2.44	0.739	Medium Spherical
Cirrus	6	400	--	--	1.32	0	0.000	1	1	1	967.48	967.48	967.48	0.814	Large Non-spherical

*The area-weighted, log-normal particle size distribution function adopted here for all spherical components is given in Equation (3), and their single scattering phase functions were calculated using a Mie code. Wavelength in nm is specified in parentheses where appropriate. For accumulation mode Asian dust, a number-weighted log-normal size distribution was adopted, and a Discrete Dipole Approximation code produced optical properties for a range of shapes and orientations designed to reproduce the observed increase in circularity with particle size [*Kalashnikova et al.*, 2003]. For coarse mode Asian dust, we preformed T-matrix calculations using an area-weighted log-normal distribution having oblate and prolate ellipsoids with a uniform distribution of aspect ratios. Modeling The asymmetry parameter (g) will generally represent non-spherical particle phase functions poorly for the purpose of calculating MISR multi-angle radiances; dust particle phase functions used here are given in the reference. The high-altitude sulfate model is based on *Wang et al.* [1989].

Table 6. Layer Optical Model Component Fraction AOT(672) for Key Multi-Platform Cases [§]

Date	April 4, 2001	April 13, 2001	April 16, 2001	April 27, 2001	May 2, 2001
Site/Platform	Oki C-130 / TO	Oki C-130 / RB	Gosan TO	Oki C-130 / TO	Gosan C-130
Layer 1					
Pollution_0.30_ssa-0.79	--	--	0.47	--	--
Pollution_0.23_ssa-0.80	--	0.45	--	--	--
Pollution_0.30_ssa-0.89	0.67	--	--	--	--
Pollution_0.23_ssa-0.91	--	--	--	0.66	--
Pollution_0.30_ssa-0.92	--	--	--	--	0.73
Asia_Accum_Dust_Grains	0.33	0.2	0.43	0.2	0.27
Asia_Coarse_Dust	--	0.05	0.1	0.14	--
Sea Salt	--	0.3	--	--	--
Layer 2					
Pollution_0.23_ssa-0.80	--	--	--	0.15	--
Pollution_0.23_ssa-0.86	--	--	0.65	--	--
Pollution_0.23_ssa-0.87	0.22	0.54	--	--	--
Pollution_0.23_ssa-0.91	--	--	--	--	0.38
Sphere_0.05_ssa-1.0	--	--	0.22	--	--
Asia_Accum_Dust_Grains	0.63	0.4	--	0.3	0.62
Asia_Coarse_Dust§	0.15	0.06	0.13	0.15	--
Cirrus	--	--	--	0.4	--
Layer 3					
Pollution_0.23_ssa-0.86	--	--	--	--	0.45
Asia_Accum_Dust_Grains	--	--	--	--	0.55
Above-Top-Layer					
Sphere_0.3_ssa-1.0	0.53	--	--	0.37	0.1
Sphere_0.5_ssa-1.0	--	0.9	0.6	--	0.4
Asia_Accum_Dust_Grains	0.32	--	0.3	0.33	0.3
High_Alt_Sulfate	0.15	0.1	0.1	0.25	0.2
Cirrus	--	--	--	0.05	--

[§] Aerosol component optical models are described in Table 5.

Table 7. Model-Observation Differences, Layer-by-Layer, for Each Constraint[§]

	Layer 1		Layer 2		Layer 3		Above-Top-Layer	
	Model-Obs.	Measure Unc.	Model-Obs.	Measure Unc.	Model-Obs.	Measure Unc.	Model-Obs.	Measure Unc.
April 4, 2001								
AOT(550)	*-0.002*	0.009	*-0.002*	0.009	--	--	*0.000*	0.013
AOT(866)	*0.000*	0.008	*0.000*	0.008	--	--	*0.000*	0.012
Sub-micr. AOT(550)	*0.003*	0.012	*0.000*	0.002	--	--	--	--
SSA(550)	*0.010*	0.020	*-0.008*	0.010	--	--	--	--
April 13, 2001								
AOT(550)	*-0.003*	0.017	*0.001*	0.017	--	--	*-0.002*	0.024
AOT(866)	*-0.001*	0.016	*0.000*	0.016	--	--	*-0.001*	0.023
Sub-micr. AOT(550)	*0.005*	0.026	*0.000*	0.005	--	--	--	--
SSA(550)	*-0.008*	0.020	*0.006*	0.020	--	--	--	--
Sub-micr. SSA(550)	*-0.009*	0.030	*0.001*	0.020	--	--	--	--
April 16, 2001								
AOT(550)	*-0.001*	0.001	*0.000*	0.001	--	--	*-0.002*	0.005
AOT(866)	*0.000*	0.001	*0.000*	0.001	--	--	*-0.001*	0.003
SSA(550)	*-0.005*	--	--	--	--	--	--	--
Sub-micr. SSA(550)	*0.002*	--	--	--	--	--	--	--
April 27, 2001								
AOT(550)	*-0.013*	0.020	*0.003*	0.072	--	--	*-0.001*	0.023
AOT(866)	*0.001*	0.017	*-0.014*	0.042	--	--	*-0.001*	0.025
Sub-micr. AOT(550)	*0.034*	0.043	*0.000*	0.011	--	--	--	--
SSA(550)	*-0.001*	0.020	*0.003*	0.010	--	--	--	--
Sub-micr. SSA(550)	*0.004*	0.020	*0.000*	0.030	--	--	--	--
May 2,								

2001								
AOT(550)	*-0.002*	0.054	*-0.001*	0.023	*-0.001*	0.024	*0.000*	0.024
AOT(866)	*-0.001*	0.033	*0.000*	0.019	*0.000*	0.023	*0.000*	0.023
Sub-micr. AOT(550)	*-0.003*	0.054	*0.000*	0.004	*0.001*	0.002	--	--
SSA(550)	*0.007*	0.020	*0.001*	0.010	*0.002*	0.010	--	--
Sub-micr. SSA(550)	*-0.001*	0.020	*-0.008*	0.020	*-0.002*	0.020	--	--

[§] AOT(672) was matched exactly for each layer.

ACE Asia: Orbit 6884, Blocks 61-68
April 04, 2001
MISR Level 1B2 RGB AN (nadir)

(37.7N, 130.7E) (37.3N, 135.0E)

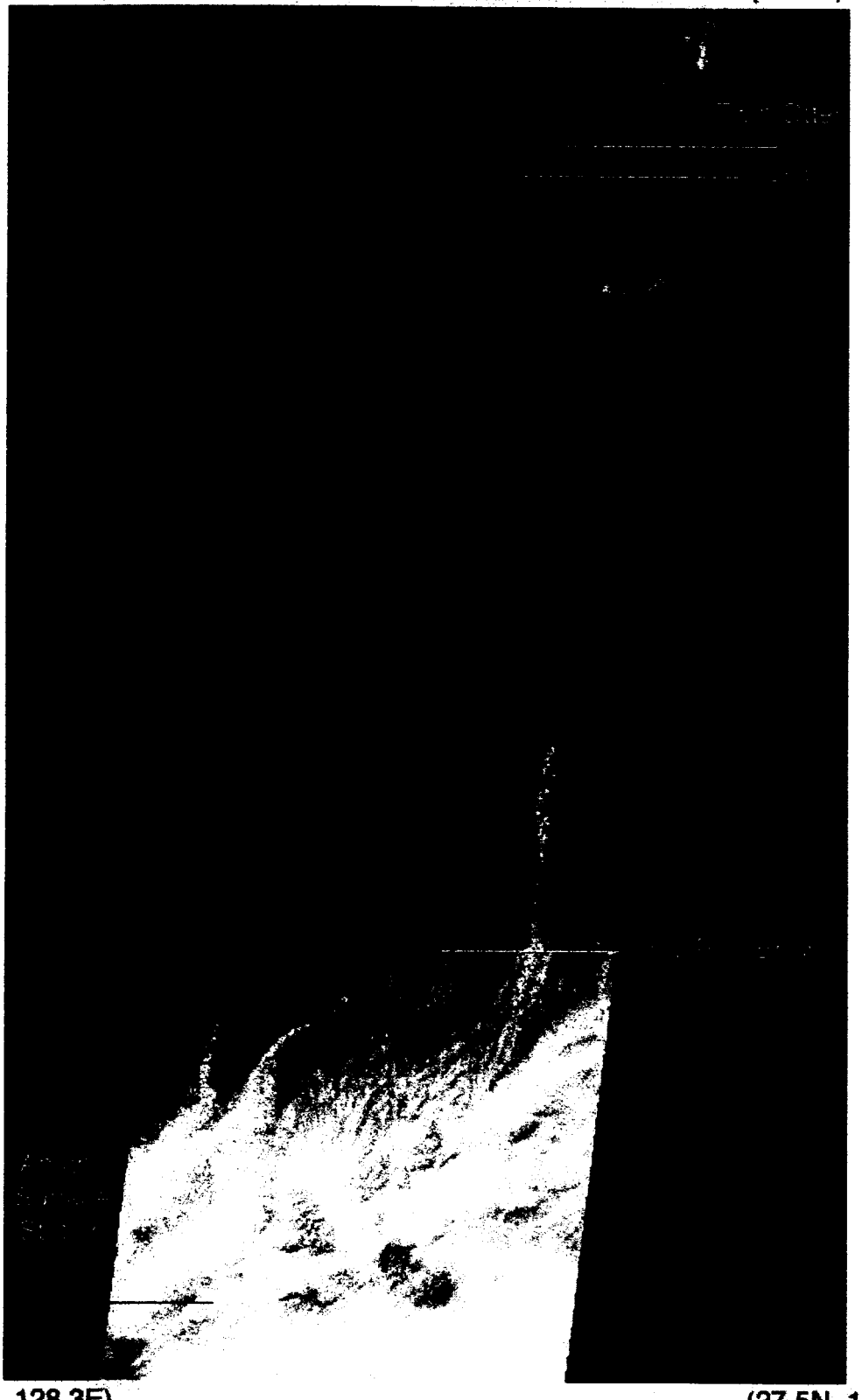

(27.8N, 128.3E) (27.5N, 132.1E)

Figure 1a

ACE Asia: Orbit 7015, Blocks 62-65
April 13, 2001
MISR Level 1B2 ELLIPSOID RGB AN (nadir)

Figure 1b

ACE Asia: Orbit 7059, Blocks 64-65
April 16, 2001
MISR Level 1B2 ELLIPSOID RGB AN (nadir)

(34.0N, 123.5E)

(33.6N, 127.6E)

(31.5N, 122.9E)

(31.1N, 126.8E)

Figure 1c

ACE Asia: Orbit 7219, Blocks 63-68
April 27, 2001
MISR Level 1B2 ELLIPSOID RGB AN (nadir)

(35.2N, 128.4E) (34.8N, 132.5E)

(27.8N, 126.6E) (27.4N, 130.4E)

ACE Asia: Orbit 7292, Block 64
May 02, 2001
MISR Level 1B2 RGB AN (nadir)

(34.00N, 123.5E)

(33.6N, 127.5E)

(32.8N, 123.1E)

(32.4N, 127.2E)

Figure 1e

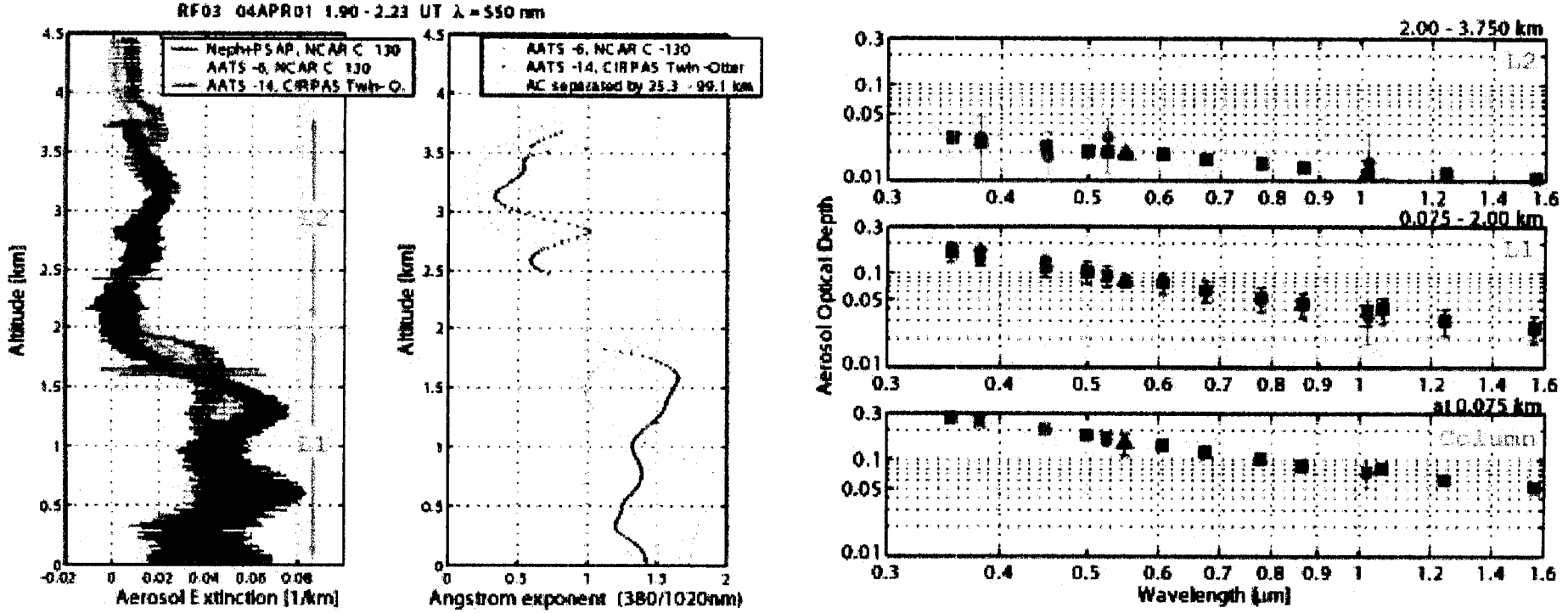
RF03 04APR01 1.90 - 2.23 UT λ = 550 nm
Neph+PSAP, NCAR C 130
AATS -6, NCAR C 130
AATS -14, CIRPAS Twin-O.
L2
L1
Altitude [km]
Aerosol Extinction [1/km]
AATS -6, NCAR C -130
AATS -14, CIRPAS Twin-Otter
AC separated by 25.3 - 99.1 km
Angstrom exponent (380/1020nm)
2.00 - 3.750 km
0.075 - 2.00 km
at 0.075 km
Column
Aerosol Optical Depth
Wavelength [µm]

Figure 2

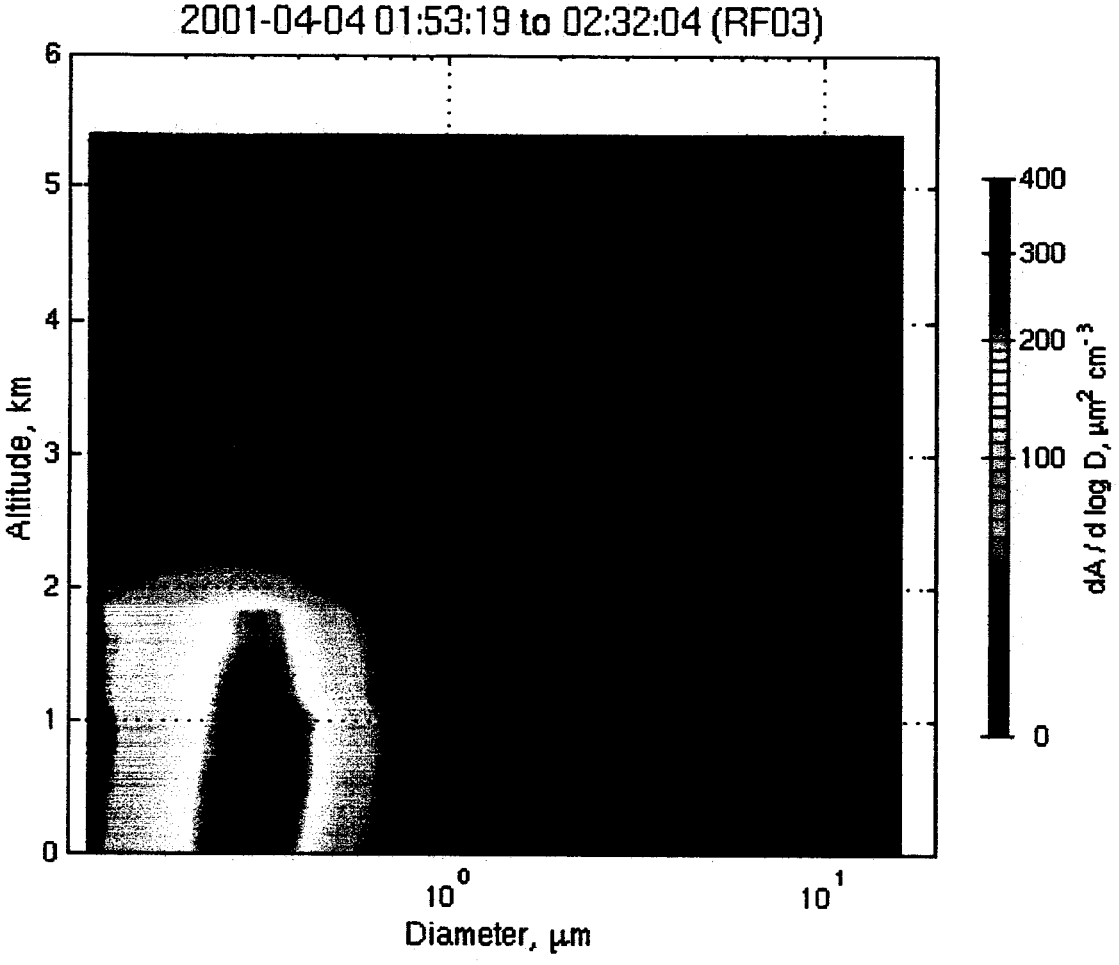
2001-04-04 01:53:19 to 02:32:04 (RF03)
Altitude, km
Diameter, µm
dA / d log D, µm² cm⁻³
0
1
2
3
4
5
6
10⁰
10¹
0
100
200
300
400

Figure 3

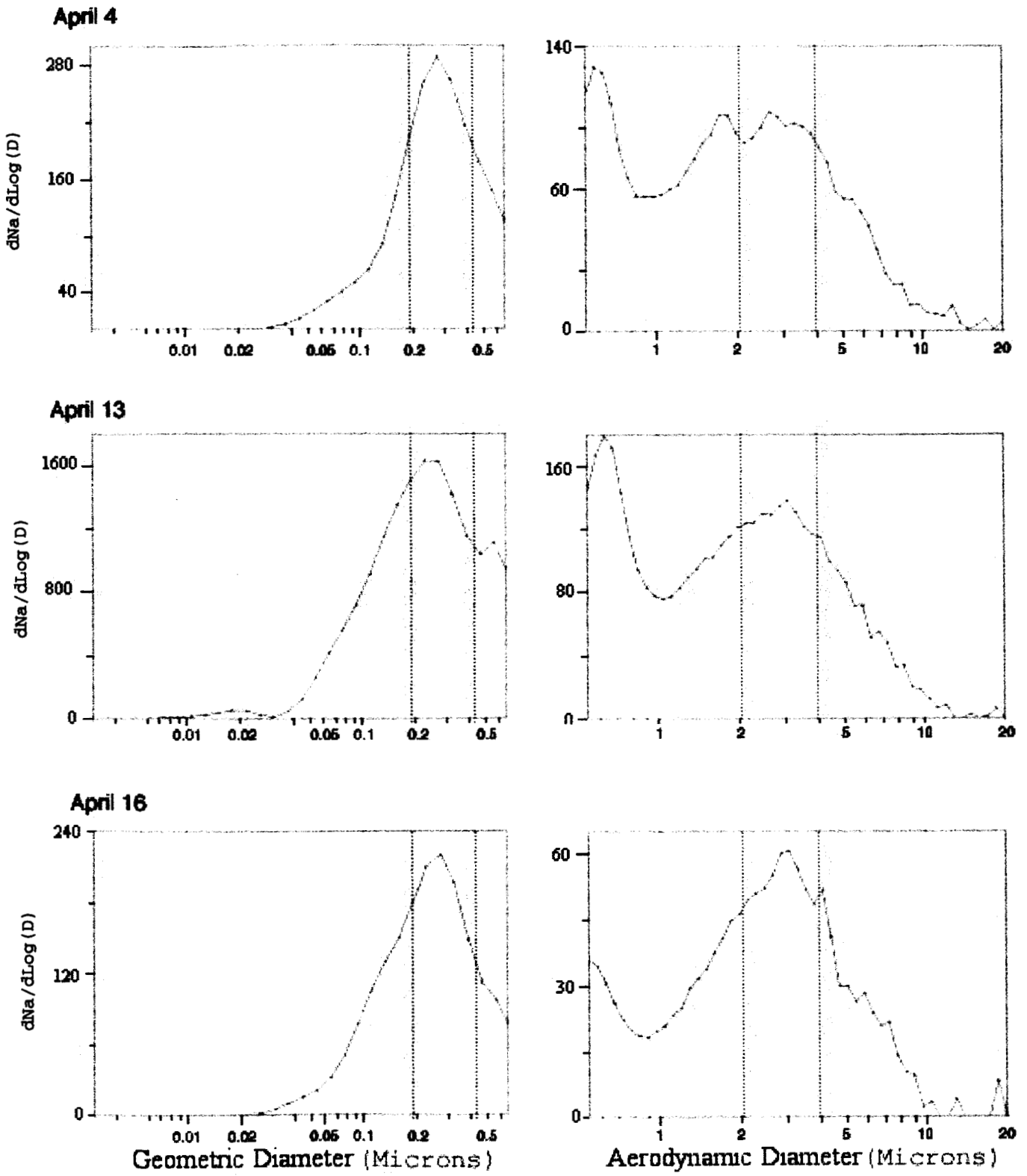
Area-Weighted Size Distributions
April 4
April 13
April 16
dNa/dLog (D)
280
160
40
140
60
0
1600
800
240
120
30
0.01
0.02
0.05
0.1
0.2
0.5
1
2
5
10
20
Geometric Diameter (Microns)
Aerodynamic Diameter (Microns)

Figure 4

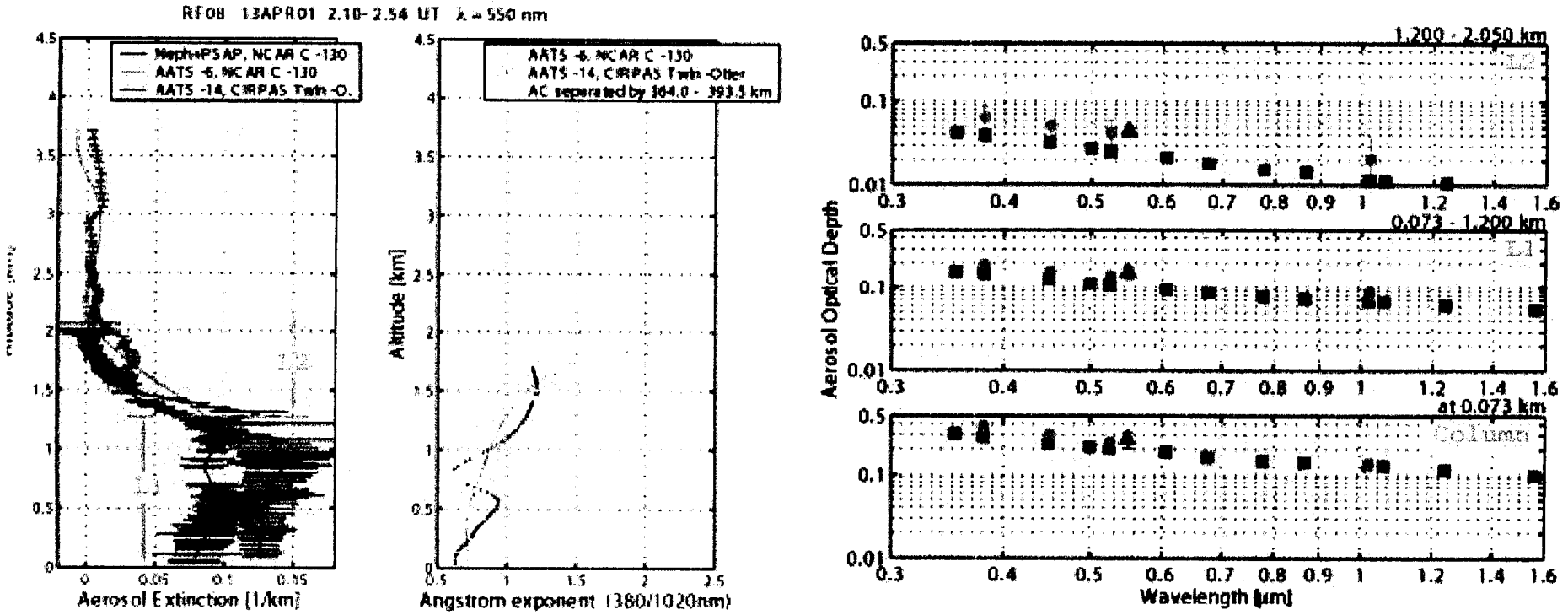
RF08 13APR01 2.10- 2.54 UT λ = 550 nm
Aeros ol Extinction [1/km]
Angstrom exponent (380/1020nm)
Altitude [km]
AATS -6, NCAR C -130
AATS -14, CIRPAS Twin -Otter
AC seperated by 364.0 - 393.5 km
1.200 - 2.050 km
0.073 - 1.200 km
at 0.073 km
Aerosol Optical Depth
Wavelength [µm]

Figure 5

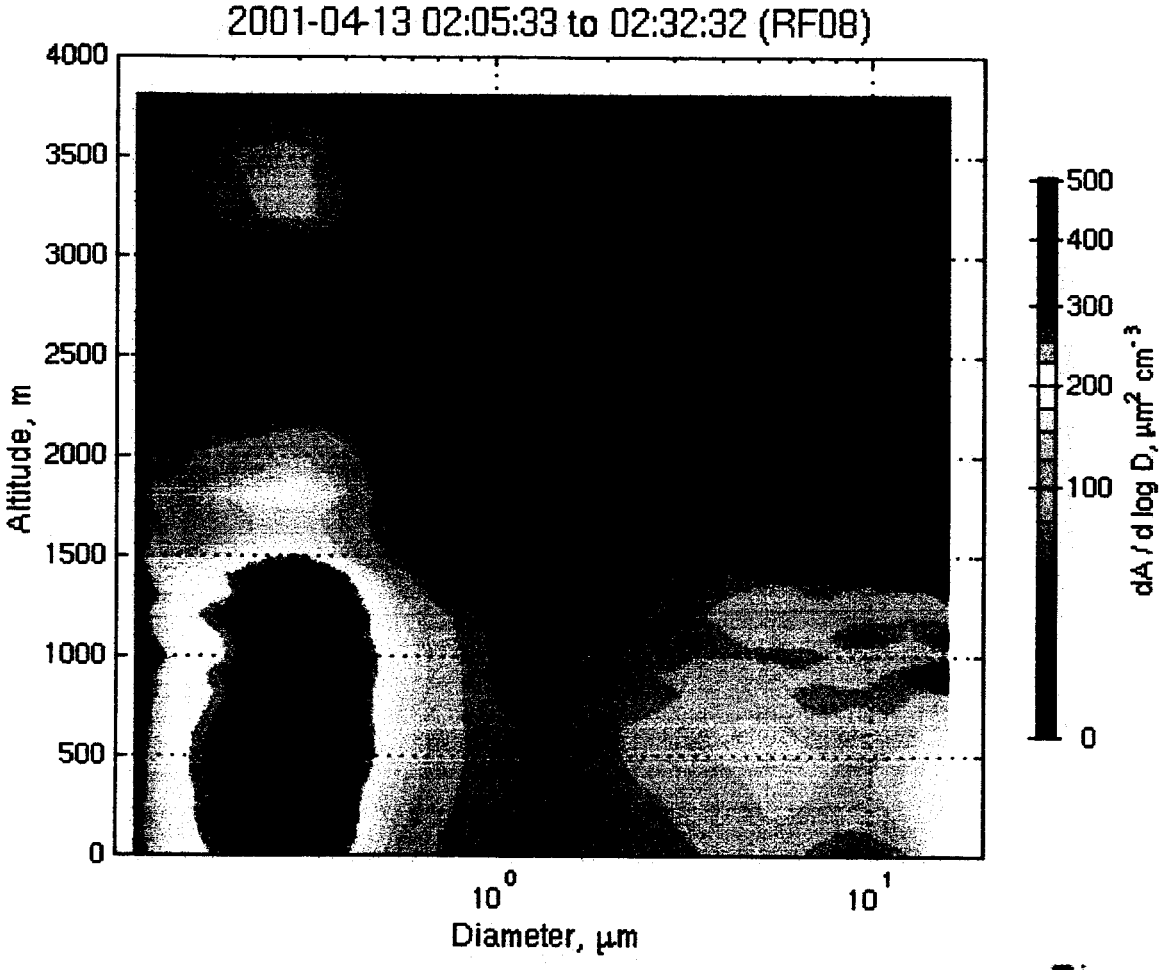
2001-04-13 02:05:33 to 02:32:32 (RF08)
Altitude, m
4000
3500
3000
2500
2000
1500
1000
500
0
10^0
10^1
Diameter, μm
500
400
300
200
100
0
dA / d log D, μm² cm⁻³

Figure 6

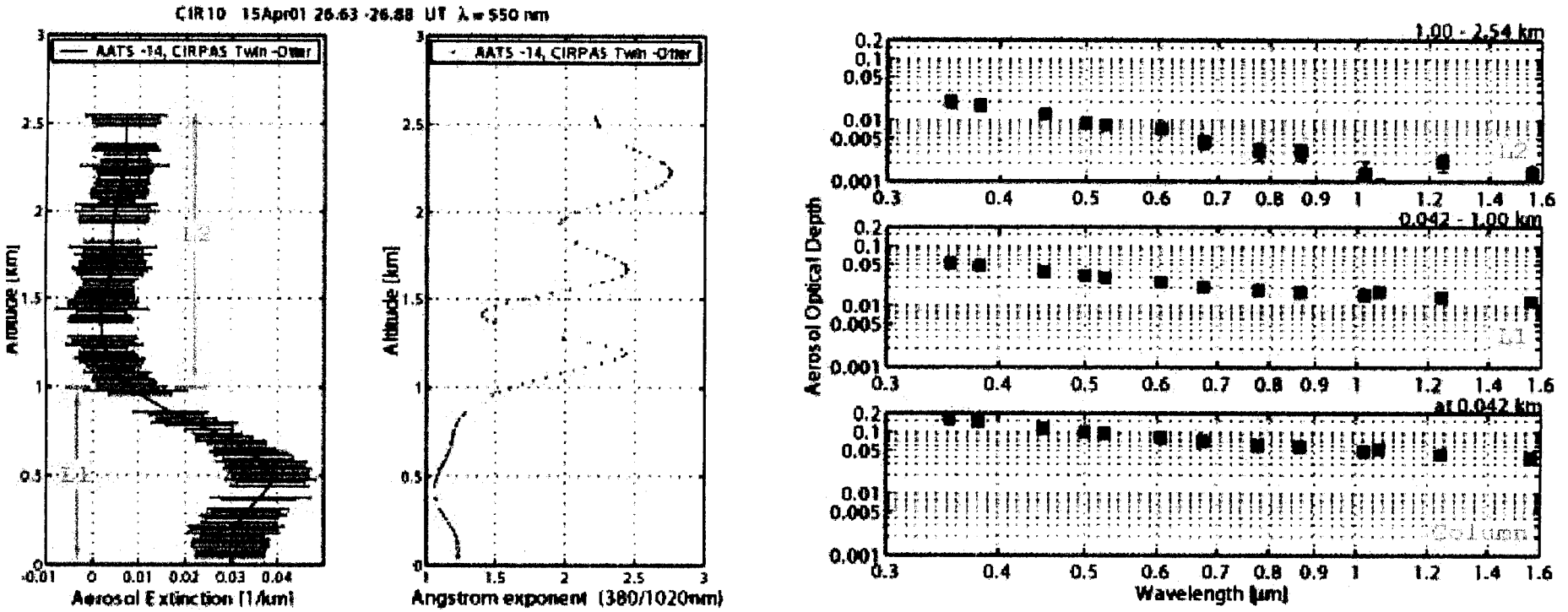
C1R10 15Apr01 26.63 -26.88 UT λ = 550 nm
AATS -14, CIRPAS Twin -Otter
Altitude [km]
Aerosol Extinction [1/km]
AATS -14, CIRPAS Twin -Otter
Altitude [km]
Angstrom exponent (380/1020nm)
1.00 - 2.54 km
0.042 - 1.00 km
at 0.042 km
Aerosol Optical Depth
Wavelength [μm]

Figure 7

Figure 8

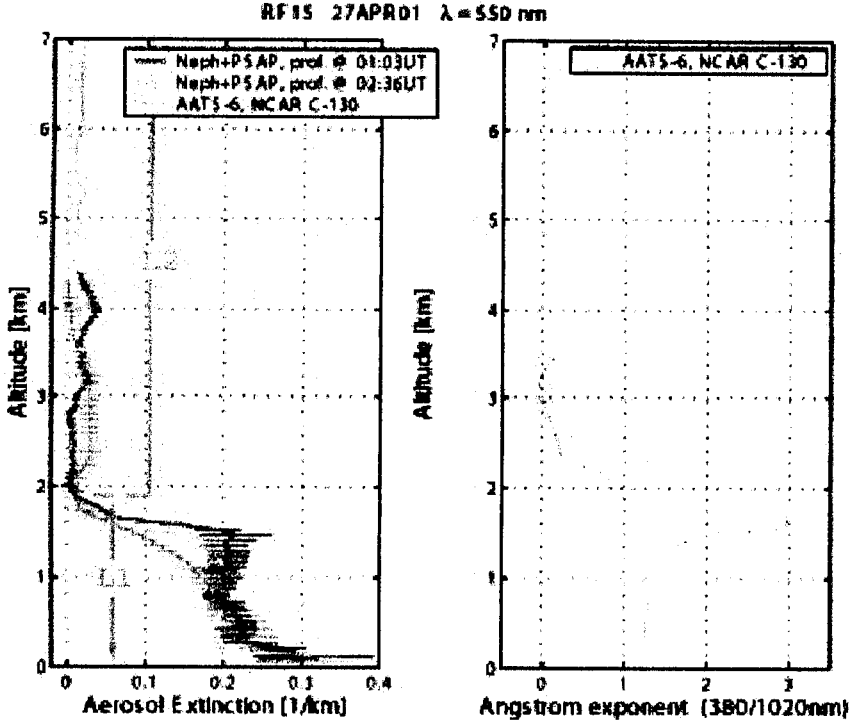
RF15 27APR01 λ=550 nm
Neph+PSAP, prof. @ 01:03UT
Neph+PSAP, prof. @ 02:36UT
AATS-6, NCAR C-130
L2
L1
Altitude [km]
Aerosol Extinction [1/km]
AATS-6, NCAR C-130
Altitude [km]
Angstrom exponent (380/1020nm)

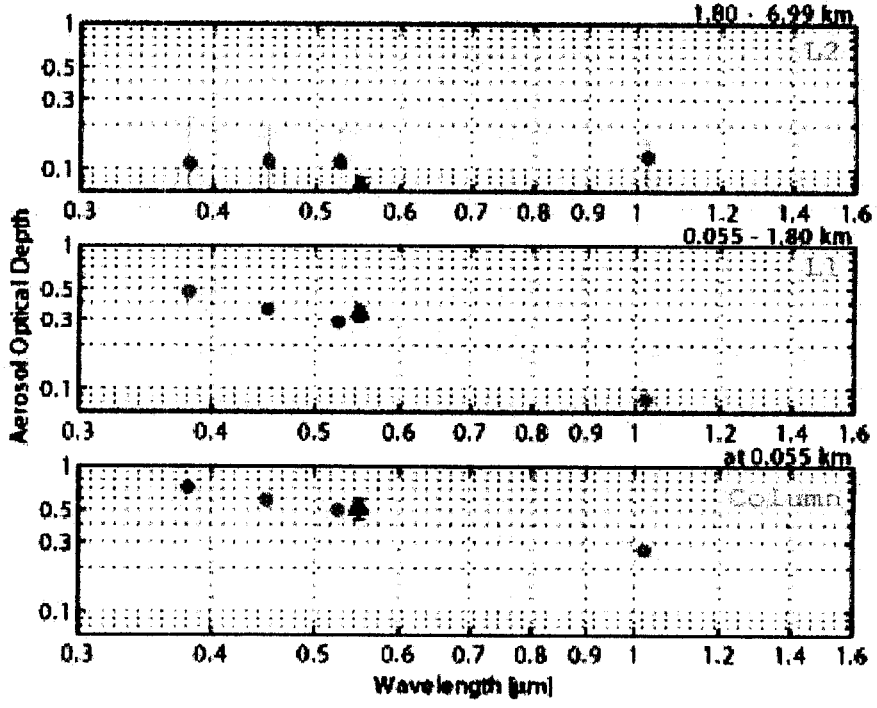
1.80 - 6.99 km
L2
0.055 - 1.80 km
L1
at 0.055 km
Column
Aerosol Optical Depth
Wavelength [μm]

Figure 9

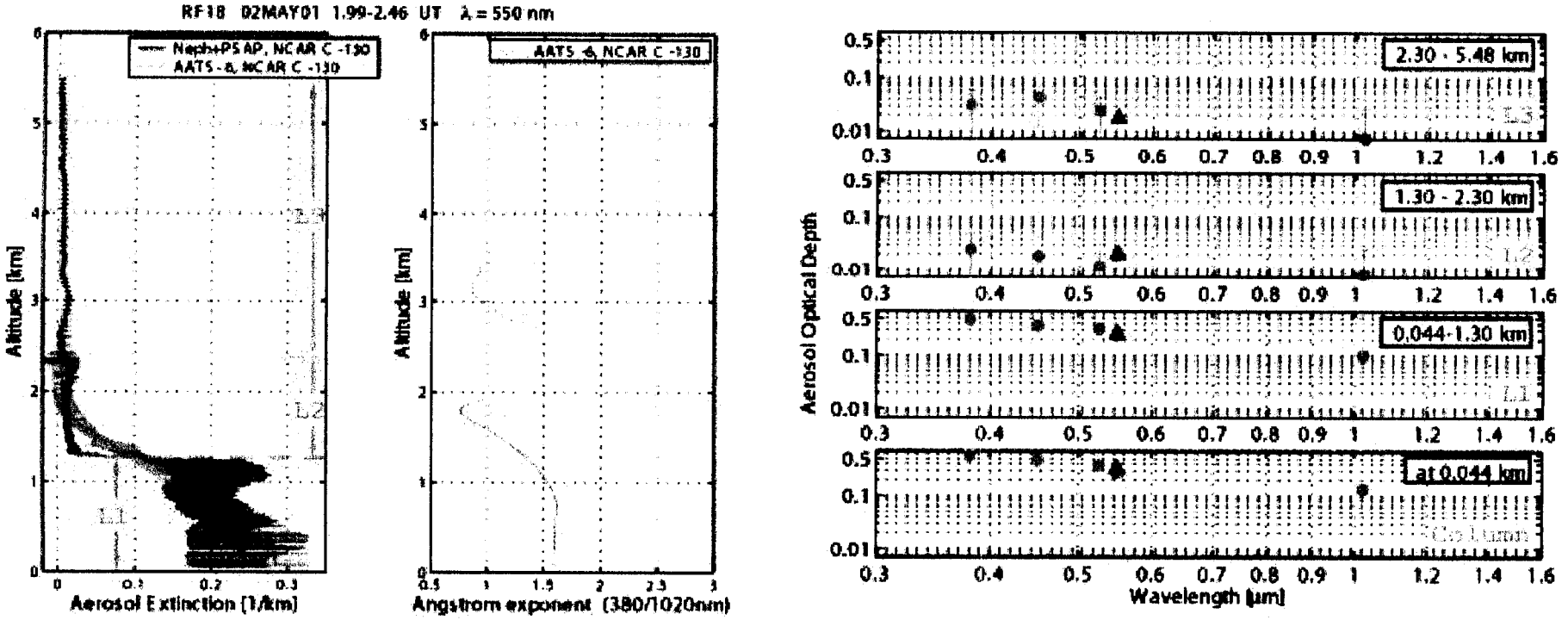
RF18 02MAY01 1.99-2.46 UT λ = 550 nm
Neph+PSAP, NCAR C -130
AATS-6, NCAR C -130
Altitude [km]
Aerosol Extinction [1/km]
Angstrom exponent (380/1020nm)
2.30 - 5.48 km
1.30 - 2.30 km
0.044-1.30 km
at 0.044 km
Aerosol Optical Depth
Wavelength [μm]

Figure 10